Quaternary Science Reviews 322 (2023) 108401

Contents lists available at ScienceDirect

Quaternary Science Reviews

journal homepage: www.elsevier.com/locate/quascirev

Refining the history of extreme coastal events in southern Newfoundland, NW Atlantic, with lake sediment archives

Krzysztof Pleskot [a,*], Les C. Cwynar [b], Cyprian Kowalczyk [a,c], Mikołaj Kokociński [c], Witold Szczuciński [a]

[a] Geohazards Research Unit, Institute of Geology, Adam Mickiewicz University, Poznań, Bogumiła Krygowskiego 12, 61-680 Poznań, Poland
[b] Department of Biology, University of New Brunswick, Fredericton, NB, E3B 5A3, Canada
[c] Department of Hydrobiology, Adam Mickiewicz University, Poznań, Umultowska 89, 61-614 Poznań, Poland

ARTICLE INFO

Handling Editor: Dr. P. Rioual

Keywords:
Newfoundland
Tsunami
Storm surge
Extratropical storm
Tropical cyclone
Hurricane
Lake sediments
ECEs
Sand peak analysis

ABSTRACT

Extreme events, including tsunamis, storm surges and hurricanes, affect the western North Atlantic coast, threatening communities and impacting ecosystems. Although these extreme coastal events (ECEs) are currently thoroughly monitored in the area, older ECEs are known only from short historical evidence. Therefore, establishing a reliable ECE history that extends more than several decades into the past requires data from geological records. This study aims to refine the existing record of ECEs on the southern Burin Peninsula (Newfoundland, Canada) that extends back to the mid-18th century by providing the first lake-sediment-based reconstruction of the event history of the Canadian province of Newfoundland and Labrador. We investigated short sediment cores collected from four shallow coastal lakes. The identification of ECEs relied mainly on lithostratigraphic evidence and peak detection of sand grain counts. Diatoms, dry bulk density, and loss-on-ignition were also analyzed. The age-depth models of the cores were based on ^{210}Pb and ^{137}Cs dating. The correlation of our records with major historical events confirmed that statistically significant sand count peaks, sand layers, and redeposited peat clasts are indicative of major ECEs. We found that the type and characteristics of ECE records depended mainly on the availability of sediment, distance from the seashore, and magnitude of the event. Although some of our ECE markers are associated with marine inundations, only slight diatom community changes were observed, contrary to what is commonly expected from the disturbance of brackish and freshwater ecosystems by major saltwater intrusions. Combined, our records indicate that at least eight ECEs occurred since the late 17th century, three of which might correlate with historically documented events, namely the 1755 CE Lisbon tsunami, the 1775 CE Great Independence Hurricane, and the 1929 CE Newfoundland tsunami. Although further investigations are required to better constrain the type and magnitude of particular ECEs, our study confirms the suitability of geological archives for improving hazard assessment in coastal regions.

1. Introduction

Extreme coastal events (ECEs), like marine inundations or extreme wind storms, are primarily associated with extra-tropical storms, hurricanes, or tsunamis. They pose major threats to the life and property of coastal communities and have a profound impact on coastal ecosystems (e.g., Cochard et al., 2008; Goto et al., 2021; Tashiro et al., 2021; Urabe and Nakashizuka, 2016). Therefore, knowledge of the type, frequency and extent of ECEs is crucial for appropriate coastal hazard assessment. Yet, historical accounts of ECEs are usually fragmentary and only rarely cover more than several centuries, necessitating a sedimentological approach to provide longer ECE records (e.g., Engel et al., 2020a; Goslin and Clemmensen, 2017; Orme et al., 2016).

Identification of ECEs in coastal sedimentary archives is possible as the events are often associated with widespread erosion and subsequent sediment transport and deposition (Donnelly et al., 2004; Goslin and Clemmensen, 2017; Nielsen et al., 2016). In particular, coastal lakes are suitable for the reconstruction of ECE histories because clastic sediments inwashed or windblown into them during ECEs are often easily distinguishable from the mostly organic sediments (Donnelly et al., 2004;

* Corresponding author.
E-mail address: krzypl@amu.edu.pl (K. Pleskot).

https://doi.org/10.1016/j.quascirev.2023.108401
Received 31 July 2023; Received in revised form 30 October 2023; Accepted 31 October 2023

Timmons et al., 2007). Furthermore, lake sediments often provide continuous records of the events that can be dated to provide a reliable inference of ECE frequency. To confirm the association of event layers in lake sediments with marine inundations, lithological characterization of sediments is commonly supplemented with various geochemical (Chagué-Goff et al., 2017), micropaleontological (Dura et al., 2016), molecular (Engel et al., 2020b), and other analyses. For instance, diatom analysis has proved useful for identifying marine inundations, which often correlate with an increased abundance of saline-tolerant diatom species (Dura et al., 2016).

Although lake records are invaluable in providing insights into the history of ECEs, the ability of a lake to record the events should be confirmed rather than assumed. This is usually achieved by correlating event layers in a dated sediment core with documented ECEs (e.g., Besonen et al., 2008; Kempf et al., 2015). As a single sediment core from a given location is not likely to provide a complete record of past events (Donnelly et al., 2004), the investigations often rely on the analysis of multiple sediment cores collected either from a single lake (intensive approach e.g. Kelsey et al., 2005) or several lakes (extensive approach e.g., Bondevik et al., 1997; Das et al., 2013).

Lake records have contributed to establishing a reliable history of ECEs for coastal areas around the world. However, a large bias is observed in the spatial representation of these studies. For instance, in the western North Atlantic basin, a database comprising over 60 reconstructions of coastal flooding events was developed for the area that stretches from the Gulf of Mexico up the East Coast of the United States, where hurricanes are frequent (Oliva et al., 2018). In contrast, major parts of the coast located more to the north, including the Canadian province of Newfoundland and Labrador, have been little investigated for the frequency of past marine inundations.

Although hurricanes Larry (September 2021) and Earl (September 2022) recently hit Newfoundland, it is generally less frequently affected by hurricanes compared to more-southerly parts of the western North Atlantic coast (Neu, 1982). Newfoundland's coasts are additionally subjected to coastal flooding from storm surges associated with extra-tropical cyclones, also referred to as winter storms (Danard et al., 2003). Moreover, the disastrous 1929 Grand Banks tsunami, which flooded the southern coast of the Burin Peninsula and killed 28 people (Ruffman, 1996a), provides evidence of tsunami hazards in Newfoundland. Apart from marine inundations, some coastal areas of Newfoundland are affected by flooding resulting from heavy precipitation, abrupt snowmelt or ice-jams (Hickman, 2006). Although it is clear that the low-lying coasts of Newfoundland are vulnerable to ECEs, the frequency of major events capable of causing substantial threats to the life and property of coastal communities is poorly constrained as it relies on incomplete written sources (Hickman, 2006; Liverman et al., 2001; Ruffman, 1996a).

Here we present the first reconstruction of ECEs for approximately the last four centuries for the southern Burin Peninsula based on sediment cores collected from four coastal lakes. The reconstruction relies

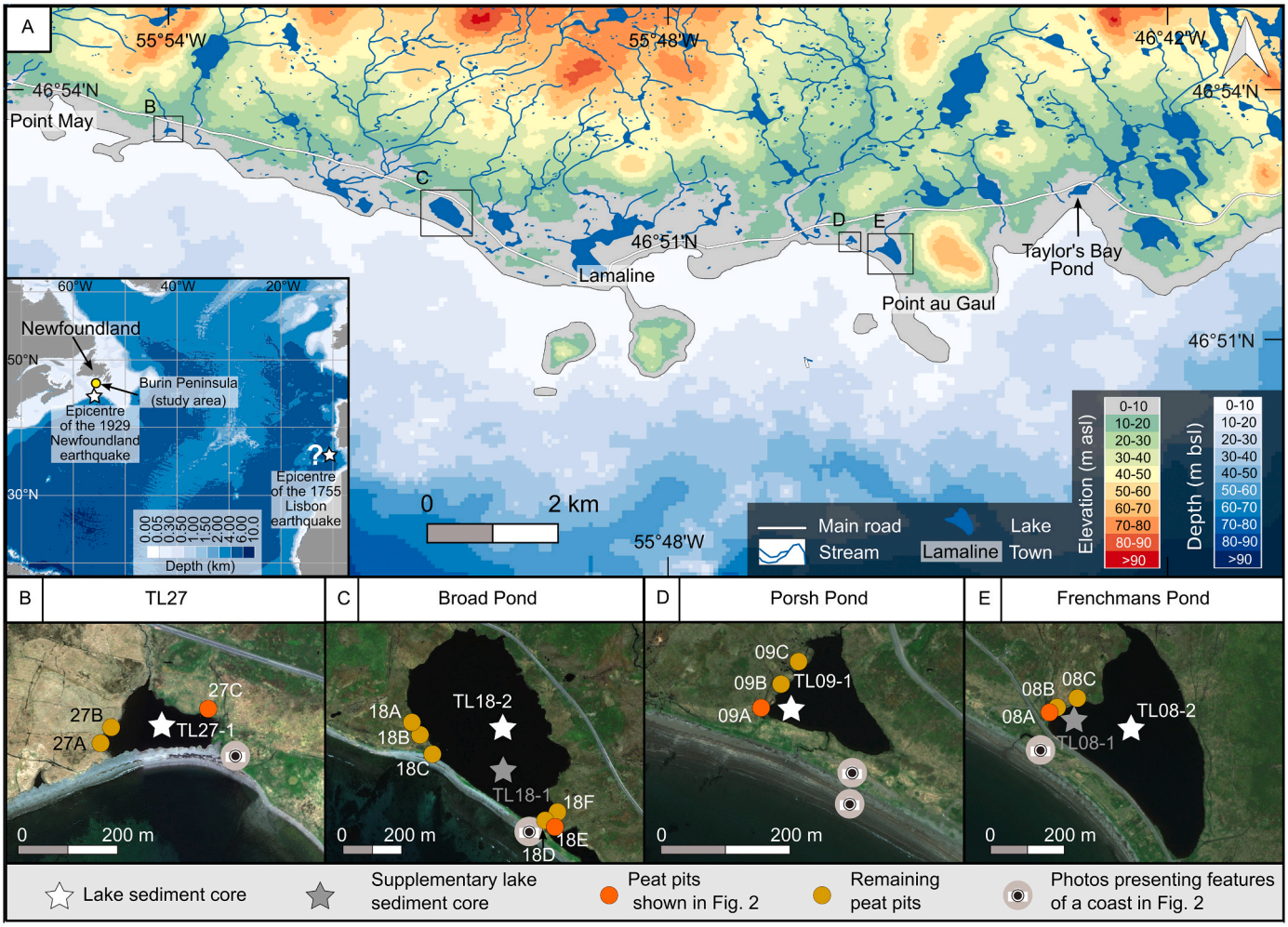

Fig. 1. (A) Location of the investigated lakes on the southern Burin Peninsula along with hypsometry of the coastal area and bathymetry of the adjacent seafloor. The inset shows the location of the study area within the North Atlantic, as well as the epicenters of two earthquakes mentioned in the text. (B–E) Satellite images of the studied lakes with marked locations of investigated peat pits and lake cores.

Table 1
List of the historically documented extreme coastal events (ECEs) in Lamaline along with a short description of the events and corresponding references. The table also includes the 1755 Lisbon earthquake which could have impacted Newfoundland according to numerical modeling studies (Barkan et al., 2009; Roger et al., 2010).

Date	Event	Description	References mentioning flooding in Lamaline
January 22, 2000	High waves superimposed on storm surge	"On 21–22 January 2000, a deep low tracked through the Maritimes causing severe impacts at numerous coastal locations. The 1.2 m storm surge coincided with perigean high tides which intensified the impact of the storm […]. On January 22, 2000, several locations within Lamaline were flooded […] Point au Gaul, Lord's Cove, and Taylor's Bay were impacted by the January 2000 event […]. The January 2000 storm caused $1 million in damages to coastal areas along the Burin Peninsula. After the January 2000 storm surge event in Lamaline, costs […] totaled $12,000". (Hickman, 2006)	Hickman (2006); Liverman et al. (2001)
December 24, 1983	High waves superimposed on storm surge	"One such event [storm surge] in Lamaline, Newfoundland on Christmas Day 1983 probably rose higher than the 1929 tsunami and occasioned fire department rescues by boat". (Ruffman, 1996a)	Ruffman (1996a); Forbes (1984) and Liverman et al. (2001) mention severe flooding in Placentia located ~145 km to the NE of Lamaline
November 18, 1929	The 1929 Newfoundland earthquake and tsunami	"In the case of the 1929 tsunami as it arrived on the Burin Peninsula, in all cases witnesses report it was first seen at about 1930 NST [Newfoundland Standard Time] as a major withdrawal […]. In the communities of Lamaline, Taylor's Bay, Lord's Cove and Port au Bras there are reports of a breaking wave arriving; up to three main pulses were seen. Many smaller pulses of the tsunami continued to affect the area for several hours after the main event". (Ruffman, 1996a)	Numerous publications describing coastal flooding along the southern Burin Peninsula (e.g., Forbes, 1984; Ruffman, 1996a; Liverman et al., 2001; Tuttle et al., 2004; Hickman, 2006)
September 9–12, 1775	Great Independence Hurricane	"Philip Tocque also briefly mentioned that "in 1775 Newfoundland was visited by a dreadful storm. The sea rose twenty feet above the usual height, which threw on shore hundreds of craft, both large and small; Additional sources eventually expanded the area known to have been affected by the storm to include Bonavista and Trinity Bays, Fogo, "Lassie" (La Scie), Conception Bay (including Northern Bay, Harbor Grace, Carbonear and Port de Grave), Placentia Bay, "Amelyne" (Lamaline), St. John's and all the Avalon Peninsula". (Ruffman, 1996b)	Ruffman (1996b); the event is commonly described to affected Burin Peninsula or Newfoundland in general, with no mention of Lamaline (e.g., Ruffman, 1996a; Liverman et al., 2001; Hickman, 2006)
November 1, 1755	The 1755 Lisbon earthquake and tsunami	"Numerical modeling confirms the possibility that reporting of wave arrival and inundation of the town of Bonavista in 1755 can be associated to the Lisbon tsunami. […] Lack of reporting in the rest of Newfoundland of the 1755 event can be readily explained by sparseness of population, community isolation, and general illiteracy amongst the outport population". (Roger et al., 2010)	No mention of flooding in Lamaline; several reports of inundation of Bonavista located ~280 km to the NE of Lamaline (e.g., Batterson et al., 1999; Liverman et al., 2001)

mainly on the lithostratigraphy of cores and sand grain counts, supported by analyses of diatoms, dry bulk density, and loss-on-ignition. Our aim was first to identify sedimentary imprints of extreme events and then use them to refine the existing ECE's history to provide a primary reference for regional coastal hazard assessment.

2. Regional setting

The topography of the Burin Peninsula is undulating with elevations exceeding 100 m above sea level (asl) in the central part of the peninsula (Fig. 1A). Coastal barrens with low-growing vegetation and sparse tree cover represented mainly by balsam fir tuckamore characterize the studied part of the peninsula (Damman, 1983). The area is mainly covered by extensive blanket bogs that are dotted with numerous ponds (Fig. 1A). A dense network of predominantly small streams with gravelly-sandy bottoms drains the blanket bog (Fig. 1A). At the outlet of some of the streams, coastal lakes and lagoons are formed.

The climate of the Burin Peninsula is strongly influenced by the proximity of the ocean. Offshore of Newfoundland, the cold southward moving Labrador current mixes with the warm northward flowing Gulf Stream. Summers are cool and foggy, with a mean temperature of 16.5 °C for the warmest month (August), whereas winters are mild, with a mean temperature of −2.7 °C for the coldest month (February) (Climate Data, 2022). Total annual precipitation averages 1634 mm with a slightly higher amount occurring during the autumn and winter months (Climate Data, 2022). Snow cover is intermittent during the winter and, in the snowiest months (January and February), it is ~10 cm thick (Damman, 1983). According to the Global Wind Atlas (Davis et al., 2023), the area experiences an average wind speed of 7.4 ms^{-1}, with prevailing western winds accounting for 17% of the annual duration.

In summer, dominant southwest winds contribute to low cyclonic activity. However, tropical cyclones from the Caribbean Sea or the Gulf of Mexico occasionally traverse the east coast of Canada and reach Newfoundland (Murty et al., 1995). The intensification of westerlies in autumn and winter is responsible for the frequent formation of extra-tropical cyclones that originate along the North American seaboard and propagate northeastward along the coast and continental shelf (Neu, 1982). Between 1979 and 2009 CE, Newfoundland experienced 35 winter extra-tropical cyclones a year on average (Plante et al., 2015).

According to the Canadian Hydrographic Service (2022), the maximum range of tides for the southern Burin Peninsula (St. Lawrence station) varies from 0.28 to 2.68 m. Over the last 3000 years, relative sea level has been continuously rising in eastern Newfoundland with a mean rate of ~0.5 mm yr^{-1} (Kemp et al., 2018). The southern Burin Peninsula is adjacent to a wide and shallow (mostly <100 m) continental shelf area called the Grand Banks of Newfoundland. The shallow offshore bathymetry favors the formation of large-amplitude storm surges as surge amplitude is inversely related to the water depth (Murty and Greenberg, 1987). The storm surges can result in coastal flooding on the southern Burin Peninsula, in particular when they are accompanied by large storm waves (Forbes, 1984).

Marine inundations are among the most-reported hazards for the Burin Peninsula. However, the frequency of these events is not well constrained for the area (Ruffman, 1996a). According to Lamaline residents (Fig. 1A), minor events occur in the town every several years

(Hickman, 2006). The frequency of major events is noticeably lower with only four documented historical cases (Table 1). The oldest documented major coastal flooding accompanied the 1775 CE hurricane, which may have been the deadliest natural disaster in Canada with the number of fatalities possibly exceeding 4000 (Ruffman, 1996b). The second-oldest documented event was a tsunami on November 18, 1929. It was caused by an earthquake-generated submarine landslide south of Newfoundland (Fig. 1A; Løvholt et al., 2019). The estimated earthquake moment magnitude was $M_W = 7.2$ (Ruffman, 1996a). The tsunami caused 28 deaths and extensive damage to the properties and infrastructure of southern Burin Peninsula communities. Tuttle et al. (2004) and Moore et al. (2007) found that the tsunami left a continuous sand layer between 1 and 25 cm thick at several locations east of Lamaline, including Point au Gaul and Taylor's Bay (Fig. 1A). At this latter site, the tsunami runup height was estimated at 8.5 m (Moore et al., 2007) and the landward distance reached at least 343 m (Tuttle et al., 2004). The two most recent major coastal flooding events affecting Lamaline occurred in 1983 and 2000 CE and were associated with high waves superimposed on storm surges. Although the documentation for the 1983 CE event is sparse, Ruffman (1996a) speculated that sea level might have risen higher than during the 1929 CE tsunami. The 2000 CE storm, in turn, is remembered for the costly damage it caused on the southern Burin Peninsula (Hickman, 2006; Liverman et al., 2001). According to numerical modeling studies, major parts of Newfoundland could also have been affected by the 1755 CE Lisbon tsunami (Barkan et al., 2009; Roger et al., 2010). Although no mention of the tsunami exists for Lamaline, the far-field impacts of the 1755 CE event are supported by eyewitness reports of the catastrophic inundation of the town of Bonavista (Batterson et al., 1999; Liverman et al., 2001) which is located ~200 km to the NE of Burin Peninsula. Apart from marine inundations, the area is also affected by flooding due to heavy precipitation, abrupt snow melts, or river ice jams. However, none of these events are of comparable magnitude to major marine inundations (Hickman, 2006). Their potential to leave sedimentary record within lake sediment archives will be elaborated upon in section 5.2.3.

As this is the first study of its type for the region, we opted to take an extensive rather than an intensive sampling approach to maximize the number of ECEs discovered. Four coastal lakes were selected (from west to east): TL27 (unofficial name), Broad Pond, Porsh Pond, and Frenchmans Pond (Fig. 1B–E, Table 2). The minimum distance of the lakes from the ocean is approximately 25–110 m and their catchments are dominated by peatlands. Relatively narrow pebble and cobble beaches, backed by a sparsely vegetated beach ridge, separate TL27 from the ocean (Fig. 2A). Similar coastal characteristics occur next to Broad Pond, except for an approximately 100 m stretch of predominantly sandy beach and a vegetated beach ridge adjacent to the SE part of the lake (Fig. 2B). The beaches at the ocean coast next to Porsh Pond and Frenchmans Pond are mainly sandy and relatively gentle, whereas the beach ridge is composed of cobbles and sand (Fig. 2C and D). The beach ridge is backed by dune remnants that reach a maximum height of ~10 m next to Frenchmans Pond (Fig. 2D).

Lake areas range from 1.7 ha (Porsh Pond) to 21.8 ha for Broad Pond (Table 2). Multiple depth soundings revealed that the shallowest lake is TL27 with a maximum measured depth of 0.5 m, whereas Broad Pond is the deepest at 3.1 m. Broad Pond, Porsh Pond, and Frenchmans Pond are slightly acidic with pHs of 6.8, 5.3, and 6.8, respectively, measured on the day of coring, while TL27 was alkaline with a pH of 9.2. Conductivity measurements indicate that TL27 and Broad Pond are slightly brackish, whereas Porsh Pond and Frenchmans Pond are freshwater. The large difference in conductivity values of TL27 waters on the day of coring and a week later, after heavy rainfall, indicates the lake can experience large salinity fluctuations (2569 vs. 1500 $\mu S\ cm^{-1}$).

3. Methods

3.1. Fieldwork

Fieldwork was conducted in August 2019. Six sediment cores were collected from the four lakes (Fig. 1 B-E; Table 2) using a Glew gravity corer (Glew, 1991); single cores were taken from TL27 (TL27-1) and Porsh Pond (TL09-1), whereas two cores were taken from each of Broad Pond (TL18-1 and TL18-2) and Frenchmans Pond (TL08-1 and TL08-2). Each core was subsampled in the field at a resolution of 0.5 (TL27-1, TL18-2, TL08-2) or 1 cm (TL18-1, TL09-1, TL08-1). The lithology of the cores was described during subsampling. On the peatlands next to the lakes (Fig. 1), several pits up to 50 cm deep were examined for the presence of event layers.

3.2. Dating

The chronology of the TL27-1, TL18-1, TL09-1, and TL08-2 cores is based on the activity of excess ^{210}Pb ($^{210}Pb_{ex}$) and verified with a penetration depth of anthropogenic ^{137}Cs. The analyses were conducted at the Institute of Geology, Adam Mickiewicz University in Poznań with a Canberra-manufactured germanium detector GX2520. Following Pennington et al. (1973) we consider the initial increase of ^{137}Cs activity to indicate the first fallout from the nuclear weapon tests in the mid-1950s (FF) and the highest activity of the isotope as indicative of the maximum deposition from the nuclear weapon tests in 1963 CE (NWT). The $^{210}Pb_{ex}$ was defined as a difference between the total ^{210}Pb and the supported ^{210}Pb ($^{210}Pb_{sup}$). The latter was taken as an average of ^{214}Pb and ^{214}Bi. In TL18-2, $^{210}Pb_{sup}$ activities were very low or below detection limits. Therefore, for the sake of consistency, $^{210}Pb_{ex}$ was calculated for all the samples using a mean value of $^{210}Pb_{sup}$ measured for the samples in which the activities were above the detection limits. The analysis was carried out on consecutive samples. To reach a minimum sediment dry weight of at least 1.5 g, subsamples from each of the cores were merged to represent 2-cm thick intervals, except for low-density topmost samples, which were merged into a 4-cm thick sample in TL18-2.

The data were analyzed using the serac package version 0.1.0 (Bruel and Sabatier, 2020) in R version 4.2.1 (R Core Team, 2022). The chronology of each core was established using three models included in serac package namely, constant rate of supply (CRS; Appleby and Oldfield, 1978), constant initial concentration (CIC; Robbins, 1978), and constant flux constant sedimentation rate (CFCS; Krishnaswamy et al., 1971). The CFCS models were computed against mass depth instead of depth to account for noticeable down-core variations in sediment densities. For TL09-1, we applied a piecewise version of the CRS model (Appleby, 2001), assuming that the sand layer at the bottom of the core corresponds to the 1929 CE tsunami. This assumption was based on the fact that, to date, the 1929 CE tsunami is the sole documented event recognized for the deposition of a distinctive sand layer on the Burin Peninsula (Tuttle et al., 2004).

3.3. Dry bulk density, loss-on-ignition, and sand grain counts

Dry bulk density (DBD), loss-on-ignition (LOI), and sand grain count data were obtained for each of the subsamples collected from all six lake cores (n = 309). DBD was determined by weighing 1-cm^3 samples after oven-drying overnight at 105 °C. Dried samples from DBD analysis were combusted at 550 °C for 4 h (LOI) to determine organic matter content (Heiri et al., 2001). All mineral grains >0.25 mm were counted from wet-sieved sediment samples of either 1 cm^3 (samples with low sand content) or 0.5 cm^3 volume (samples with high sand content). Prior to sieving, the samples were left for 24 h in 40 ml of 10% KOH to

Table 2
Basic characteristics of the lakes and the lake sediment cores.

	Lake ID					
	TL27	Broad Pond		Porsh Pond	Frenchmans Pond	
Area (ha)	1.9	21.8		1.7	12.8	
Max. Depth (m)	0.5	3.1		1.5	2.1	
Min. Distance to the sea (m)	~25	~30		~65	~110	
Outflow	no	no		yes	yes	
Conductivity (μS cm^{-1})	2569 (1500)[a]	1430		126	115	
pH	9.2	6.8		5.3	6.8	
No. of cores	1	2		1	2	
Core ID	TL27-1	TL18-1 (supplementary core)	TL18-2	TL09-1	TL08-1 (supplementary core)	TL08-2
Core latitude (N)	46°53′31.128	46°53′31.128	46°53′31.128	46°53′31.128	46°53′31.128	46°53′31.128
Core longitude (W)	55°53′59.495	55°53′59.495	55°53′59.495	55°53′59.495	55°53′59.495	55°53′59.495
Coring depth (m)	0.5	2.9	3.1	1.4	1.7	2.1
Core length (cm)	36.5	29.0	43	33	21	34
Short-lived isotope dating of sediment core	yes	no	yes	yes	no	yes

[a] The value obtained from the second measurement taken a week after the coring. All the remaining values are the conductivity reads from the coring dates.

deflocculate the sediment and then for an additional 1 h in a 50/50 mixture of 10% KOH and bleach to enhance the visibility of mineral grains. Diagrams presenting DBD, LOI, and sand grain counts were plotted with R using tidypaleo 0.1.2 (Dunnington et al., 2022).

3.4. Peak detection analysis of sand grain counts

To identify statistically significant peaks in sand grain counts, we performed peak detection analysis following the method described by Higuera et al. (2010) for charcoal counts. The bottom sand layer from TL09-1 was excluded from the analysis and was considered an event layer without further statistical examination. Peak detection comprised several steps. First, the records were resampled to obtain equally spaced sand accumulation rate series. In each record, the spacing in resampled series equalled the median age difference between the samples in the raw sand-grain-count records as derived from the adopted ^{210}Pb-based age-depth models. For TL27-1, TL18-2, and TL08-2 we used age estimates from the CFCS model, whereas for TL09-1 we used CRS piecewise model output. Second, the resampled series were detrended based on trend estimations with a generalized additive model (GAM). Third, we applied a Gaussian mixture model to separate noise from peak components in the detrended sand accumulation rate records. We choose a threshold value for peak components to correspond to the 99.9th percentile of the noise population. Finally, the identified peaks were tested for the probability that they arose from the same distribution as the non-peak sample with the lowest value among the previous five samples. All peaks for which the probability was lower than 0.05 were marked as statistically significant. The peak detection analysis was performed using the tapas package version 0.1.2 (Finsinger and Bonnici, 2022) in R. For trend estimation with GAM, we used the mgcv package version 1.8.40 (Wood, 2017).

3.5. Diatom analysis

We analyzed diatoms for TL27-1 (n = 12), TL18-2 (n = 46), TL09-1 (n = 11), and TL08-2 (n = 11). The diatom composition was examined for the possible enrichment of marine or brackish species at the depths corresponding with sand peaks in comparison to samples from adjacent layers. One-cm^3 samples were prepared according to the method of Battarbee (1986). Bulk sediment was treated with peroxide at 92 °C to remove organic matter after which the material was centrifuged at 3000 relative centrifugal force (RCF) and mounted into Naphrax for microscopic slide preparation. We identified 400 valves in each sample using an OLYMPUS BX51 microscope with Nomarski contrast under 1000x magnification. The taxa were grouped according to their salinity preferences (marine, brackish, euryhaline, and freshwater). Species with unknown salinity preference were categorized as 'undifferentiated'. The identification and classification of diatoms followed several keys and taxonomic monographs (Bąk et al., 2012; Krammer and Lange-Bertalot, 1991; Reichardt, 1999; Witkowski et al., 2000). The taxonomic nomenclature was updated following AlgaeBase (Guiry and Guiry, 2023). The diatom diagrams were plotted with R using rioja 0.9–26 (Juggins, 2020).

3.6. Principal component analysis of diatom data

To determine the compositional relationship between the samples corresponding to the sand peaks and the remaining samples, we performed principal component analysis (PCA) on the diatom data from TL18-2. Prior to the analysis, the species data were square-root transformed. The analysis was run in R using vegan version 2.6–2 for computation (Oksanen et al., 2022) and the ggvegan package version 0.1–0 for plotting the PCA biplot (Simpson, 2019).

3.7. Calculation of lake wave-base

To evaluate the influence of lake sediment resuspension driven by wind-generated waves, we computed wave bases (WB) following the method of Patterson et al. (2020) using the formula:

$$WB = 0.39 \times T^2 \quad (1)$$

where T is the period of a wave in seconds, based on the equation of Smith and Sinclair (1972):

$$\frac{gT}{w} = 0.46\left(\frac{gF}{w^2}\right)^{0.28} \quad (2)$$

where g is the acceleration due to gravity in m s^{-1}, w is the wind speed in m s^{-1}, and F is the fetch length in meters. We calculated the fetch length distances to the coring sites from the lake shores in various directions, namely N, NE, E, SE, S, SW, W, and NW. We employed three different scenarios for calculating WB, using average, storm, and extreme wind speed values. Average conditions were defined as wind speeds matching the mean annual speed of 7.4 m s^{-1} as derived from Global Wind Atlas (Davis et al., 2023). Storm conditions were represented by a wind speed of 28.6 m s^{-1}, a lower threshold for storm winds according to NOAA (2023), while extreme wind speed of 49.6 m s^{-1} is equivalent to the lower threshold value for a major hurricane (category 3 on the Saffir-Simpson scale). In the extreme scenario, the value exceeds 47.8 m s^{-1}, corresponding to the highest wind speed measured in southern Burin Peninsula during the passage of Hurricane Michael in 2000 (Bowyer, 2014).

Fig. 2. Features of the coast and characteristics of the event layers in the peat pits by the investigated lakes (photo: K. Pleskot – all). For locations of the photos see Fig. 1.

4. Results

4.1. Dating

The activities of $^{210}Pb_{ex}$ and ^{137}Cs along with age-depth models for TL27-1, TL18-2, TL09-1, and TL08-2 are presented in Fig. 3. Each of the cores revealed an exponential decrease of $^{210}Pb_{ex}$ activity with depth down to the core bottom (TL09-1 and TL08-2) or the maximum depth analyzed (TL27-1 and TL18-2). The maximum $^{210}Pb_{ex}$ activities were high, in the range of 790 and 1233 mBq g^{-1}, except for TL27-1 with a maximum of 82 mBq g^{-1}. The highest r^2 for the exponential fit curve was for TL09-1 (0.98) followed by TL08-2 (0.97), TL18-2 (0.96), and TL27-1 (0.77).

The initial increase of ^{137}Cs activity, presumably associated with the first fallout in the mid-1950s (FF), can roughly be positioned at 16–20 (TL27-1), 10–14 (TL18-2), 22–26 (TL09-1), and 20–24 (TL08-2) cm. Clear ^{137}Cs peaks related to the 1963 maximum deposition of the radionuclide from nuclear weapon tests (NWT) were found in TL18-2 (54.6 mBq g^{-1}) and TL08-2 (147.7 mBq g^{-1}) at depths of 8–10 and 16–19 cm, respectively. In TL09-1, there were two ^{137}Cs peaks with the larger peak at 18–22 cm marked as NWT (65.5 mBq g^{-1}) and the smaller one (42.3 mBq g^{-1}) at 10–12 cm. The ^{137}Cs profile of TL27-1 lacked a clear peak. The highest activities of the radionuclide in the core (31.1 mBq g^{-1}) were at depths between 6 and 8 cm.

For TL27-1, profiles of constant flux constant sedimentation rate (CFCS) and constant initial concentration (CIC) age models are similar (Fig. 3A). However, CIC differed in showing several age reversals, most notably below 20 cm depth. The constant rate of supply (CRS) model revealed consistently younger ages than CIC and CFCS, likely due to incomplete $^{210}Pb_{ex}$ inventory, as the dating horizon (the sediment depth with no $^{210}Pb_{ex}$) was not reached. A depth of ^{137}Cs FF closely corresponded with the output of CFCS and CIC models and not with CRS. Considering the above limitations, the CFCS age model was used as the most accurate. It resulted in a mass accumulation rate (MAR) of 0.04 ± 0.006 g cm^{-2} yr^{-1}. Given this value, the bottom of core TL27 (36.5 cm) corresponds with ~1908 CE (the model uncertainty within the range of 1893–1923 CE).

For TL18-2, the profiles of CFSC, CIC, and CRS age models are similar, and agree with ^{137}Cs FF and NWT age markers (Fig. 3B). Large uncertainties that propagate downward occurred in the CIC and CRS models below 15 cm. Therefore, the CFCS age model was chosen. The CFCS model revealed a MAR of 0.01 ± 0.0008 g cm^{-2} yr^{-1}. Given this value and assuming a stable sediment accumulation rate for the period older than approximately 150 years ago (the maximum limit of ^{210}Pb method), the bottom of core TL18-2 (43 cm) corresponds with approximately 1634 CE (the model uncertainty within the range of 1613–1652 CE).

For TL09-1, the CFCS, CRS, and CIC models revealed similar age-depth profiles (Fig. 3C). The CRS piecewise model, that was forced to a date of 1929 CE for the sandy bottom of the core, agrees with the remaining models down to ~20 cm depth. The assumption of the tsunami origin of the layer is supported by observations of a single sand layer in the peat trenches nearby (Fig. 2C) and historical descriptions from the site (Point au Gaul). The NWT matched the age estimates of all the models, whereas FF agreed only with CRS piecewise, which was therefore used. The CFCS calculated MAR is 0.02 ± 0.0008 g cm^{-2} yr^{-1}.

For TL08-2, the outputs of the CFCS, CIC, and CRS models were similar and the shifts between the profiles rarely exceeded a few years, except for CRS being shifted toward noticeably older ages at the very bottom of the core (Fig. 3D). Overall, the best agreement between the cesium-based age markers (FF and NWT) and the models was found for the CFCS model, which was used as the most accurate. The CFCS-based MAR is 0.03 ± 0.002 g cm^{-2} yr^{-1} and core bottom sediment (34 cm) corresponded with ~1904 CE (the model uncertainty within the range of 1898–1909 CE).

4.2. Lithology, dry bulk density, loss-on-ignition, and sand grains counts

The lithology, DBD, LOI, and sand grains counts for the dated cores are presented in Fig. 4, whereas the data for supplementary cores TL18-1 and TL08-1 are shown in Fig. 5.

The TL27-1 core was 36.5 cm long and consisted of homogenous brown gyttja with peat intraclasts at ~20–21 cm (~1962 CE) and in the bottommost 2.5 cm (34–36.5 cm; before ~1916 CE; Fig. 4A). The peat intraclasts at the bottom were large and constituted a major part of the core, whereas peat intraclasts from ~20 to 21 cm were noticeably smaller with a maximum length of approximately 1 cm. DBD values were relatively stable over most of the core, ranging from 0.1 to 0.16 g cm^{-3}. Only the topmost 2.5 cm revealed a sharp DBD drop. The depths containing peat intraclasts had the highest LOI values (>65%). For the rest of the core, LOI decreased upward from ~60 to ~40%. However, in the topmost 2.5 cm, LOI rebounded to ~50%. The number of sand grains was very low throughout TL27-1 with many samples having no grains. The highest number of 16 sand grains cm^{-3} occurred at 17.75 cm (~1971 CE).

The TL18-1 core was 29 cm long (Fig. 5A). It consisted of poorly sorted sand with pebbles below 27 cm and at 17–23 cm, and homogenous brown gyttja at 23–27 cm and from 17 cm upward. DBD and sand content were substantially lower in gyttja compared to sand layers (generally <0.15 vs. mostly >0.75 g cm^{-3} and 6–866 vs. 1250–13,130 grains cm^{-3}, respectively). LOI was generally high with values mostly exceeding 40%, and decreased to 2% in sand layers.

Core TL18-2 was 43 cm long and consisted of homogenous brown gyttja that contained rounded pebbles at 35–36 cm (~1743 CE; Fig. 4B). Overall, DBD decreased upward from the bottom, where it exceeded 0.2 g cm^{-3}, reaching a minimum of 0.04 g cm^{-3} in the topmost sample. However, several positive excursions occurred, most notably where pebbles were found (35–36 cm). The LOI profile was roughly opposite to that of DBD with values ranging between ~20% at the bottom and ~70% at the top. The number of sand grains was generally low with only a few present in many samples. However, several positive excursions occurred at 5.5–6, 23–24, 31.5–32, 35–36, 40–40.5, and 42–43 cm (~1995, 1864, 1792, 1743, 1682, and 1633 CE, respectively). The sand peak at 35–36 cm (~1743 CE) was the highest with 506 grains cm^{-3}.

Core TL09-1 was 33 cm long (Fig. 4C). It contained a 2 cm thick sand layer at the bottom that was overlain by homogenous brown gyttja. DBD was mostly stable with values ranging between 0.10 and 0.125 g cm^{-3}. The exceptions were the bottom sand layer, where DBD exceeded 0.6 g cm^{-3}, and the topmost 5 cm for which an upward decrease in density was observed with a minimum of 0.01 g cm^{-3} in the topmost sample. Below 15 cm, LOI values fluctuated markedly showing a distinct minimum at the sand layer (13%) and 27–28 cm (40%), and distinct maxima at 30–31 (74%) and 23–24 (68%) cm. From 15 cm upward LOI was generally stable with values within the range of 50–61%. The number of counted sand grains was high in a sand layer at 31–33 (1929 CE; 2220 grains cm^{-3}), at 27–29 (~1933 CE; 408 grains cm^{-3}), and 20–23 cm (~1956 CE; 172 grains cm^{-3}). In the remaining samples, the sand counts were low (mostly <50 grains cm^{-3}), with a slight positive excursion at 14–15 cm depth (~1983 CE).

The TL08-1 core was 21 cm long (Fig. 5B). Between 16 cm and the bottom, the core was composed of weakly decomposed brown peat with numerous remains of rootlets. Above the peat, a poorly sorted sand layer containing single pebbles was overlain by homogenous brown gyttja that stretched from 6 cm upward. DBD and sand content were low for peat and gyttja, and high for the sand layer (0.05–0.34 vs. 0.52–1.04 g cm^{-3} and 26–1,138 vs. 1,472–6,012 grains cm^{-3}, respectively). The highest LOI values were reported for peat (49–55%) followed by gyttja (11–36%) and sand (below 10%, except of 11–12 cm depth where LOI reached 22%).

Core TL08-2 was 34 cm long and composed entirely of homogenous brown gyttja (Fig. 4D). DBD fluctuated between 0.11 and 0.16 g cm^{-3} below 10 cm depth (~1995 CE) and decreased upward reaching a

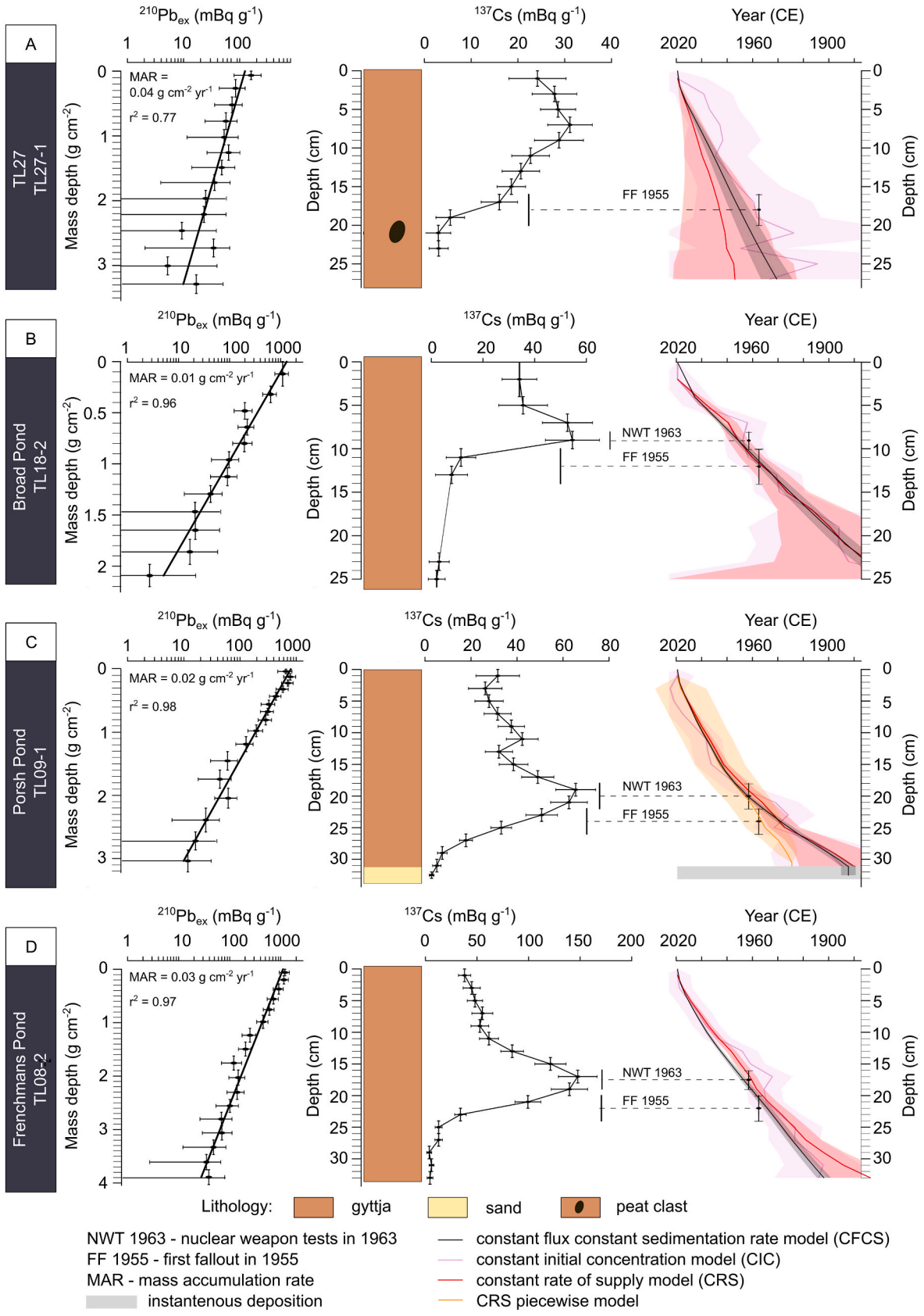

Fig. 3. Short-lived radionuclides measurements and age-depth models for the four investigated sediment cores. From left to right for each of the cores are shown: $^{210}Pb_{ex}$ activity (semilogarithmic plot) against mass depth, ^{137}Cs activity against depth, and the three various age-depth models: CFCS, CIC, and CRS. The vertical error bars refer to analyzed sediment sample mass depth range ($^{210}Pb_{ex}$ plot) or thickness (^{137}Cs plot), while the horizontal bars depict 2-sigma uncertainty.

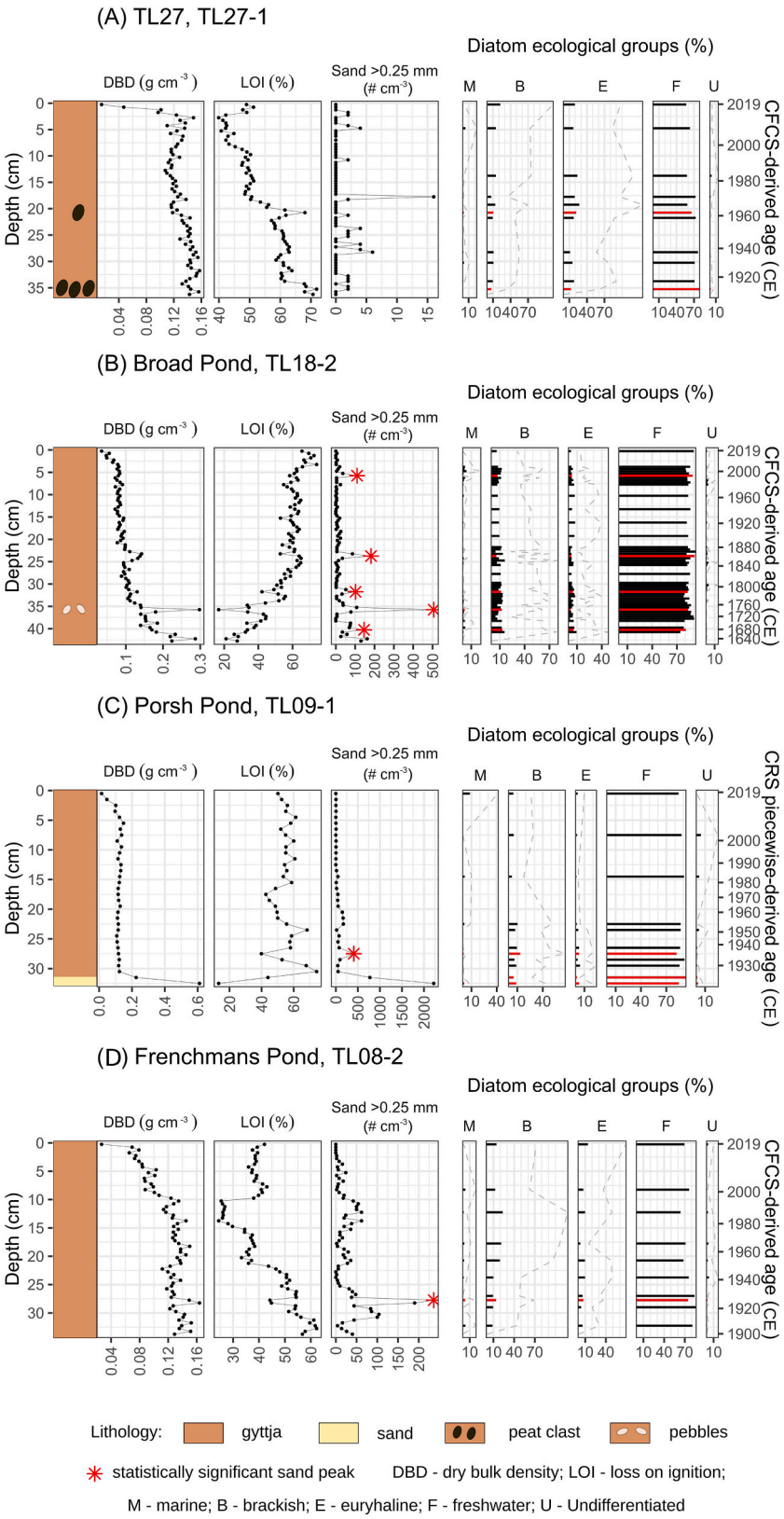

Fig. 4. Basic characteristics of the investigated sediment cores (lithology, dry bulk density, loss-on-ignition, and sand grain counts) along with the contribution of the diatom salinity groups projected on the depth scale, and age scale (on the right). The red bars in plots showing diatom salinity groups mark the samples corresponding to the sedimentary event markers. The model selected for age estimation is indicated in the label of the age scales. Identification of the statistically significant sand peaks was performed based on peak detection analysis described by Higuera et al. (2010). The results of the peak detection analysis are presented in Fig. 6.

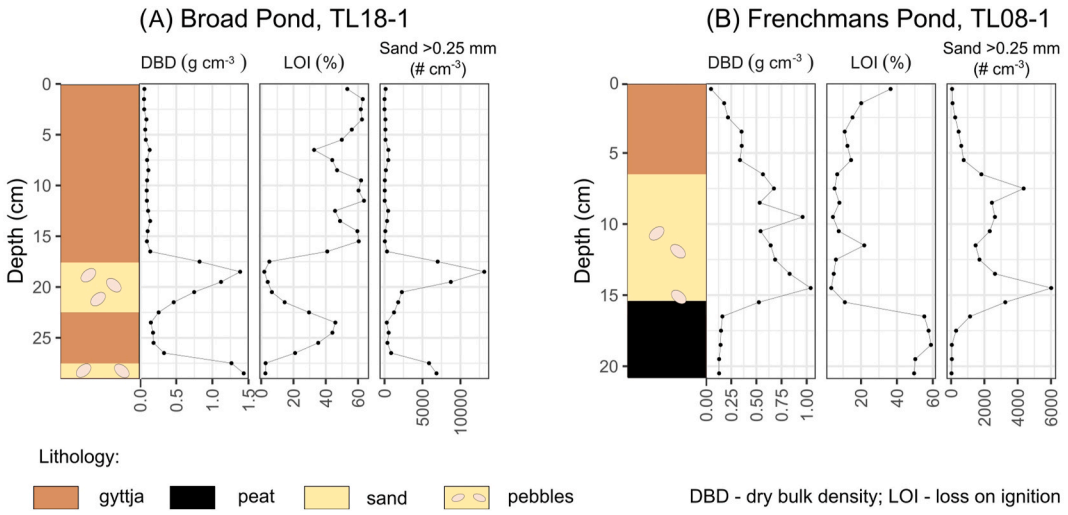

Fig. 5. Lithology, dry bulk density, loss-on-ignition, and sand grain counts for the supplementary sediment cores collected from Broad Pond (TL18-1; A) and Frenchmans Pond (TL08-1; B).

minimum of 0.03 g cm^{-3} in the topmost sample. LOI was highly variable. Below 21 cm (~1952 CE) values were the highest (mostly >50%) but a noticeable drop to 44% was at 27.5–28.5 cm (~1924 CE). Above 21 cm depth, LOI dropped in two steps, first, to ~35%, and then at 15 cm (~1977 CE) to ~26%. LOI rebounded in the topmost 10 cm to >35%. Sand grain counts showed a single distinct peak (236 grains cm^{-3}) at 27.5–28.5 cm (~1924 CE). Apart from this peak, the sand grain profile revealed mostly smooth changes indicating elevated content (>20 grains cm^{-3}) at 10–15.5, 18.5–21.5, 25.5–31.5, and 33–34 cm.

4.3. Peak detection analysis in sand grain count records

Statistically significant peaks in sand grain counts are marked in Fig. 4, while detailed results of peak detection analysis are shown in Fig. 6. The threshold values in detrended sand accumulation rate records were −0.2, 4.4, 37.6, and 6.3 grains cm^{-2} yr^{-1} for TL27-1, TL18-2, TL09-1, and TL08-2, respectively. For TL27-1, the threshold value was crossed by nine values, but none was statistically significant. For TL18-2, we found five statistically significant peaks at 40–40.5, 35–36, 31.5–32, 23–24, and 5.5–6 cm depths. Considering the age uncertainties of the CFCS model, the age ranges for the peaks were 1657–1700, 1721–1771, 1775–1806, 1849–1879, and 1989–1999 CE. One statistically significant peak occurred in each of TL09-1 (27–28 cm) and TL08-2 (27.5–28.5 cm). Given the age-depth model uncertainties, the age ranges for the peaks were 1930–1946 (TL09-1; CRS piecewise model) and 1918–1931 CE (TL08-2; CFCS model).

4.4. Diatom composition

A total of 124, 147, 120, and 123 taxa were identified for TL27-1, TL18-2, TL09-1, and TL08-2, respectively. In all the records and at all depths, freshwater diatoms dominated (contribution of >60%), whereas marine diatoms occurred in low abundances (rarely exceeding 3%) or were absent (Figs. 4 and 7). The contribution of brackish, euryhaline, and undifferentiated species varied between the lakes. Although the proportion of these groups fluctuated in TL18-2, TL09-1, and TL08-2, brackish diatoms generally dominated euryhaline and undifferentiated ones (Fig. 4B–D and 7 B-D). In TL27-1, brackish and euryhaline diatoms occurred in similar abundances that ranged between 7 and 24%, while undifferentiated species did not exceed 3% (Fig.. 4A and 7A). *Pseudostaurosira elliptica* and *Stauroforma exiguiformis* were the two most abundant freshwater species in each record (Fig. 7). Some samples revealed notable amounts of *Navicula meniscus* (TL18-2, TL08-2), *Stephanocyclus meneghinianus* (TL27-1, TL18-2, TL08-2), *Diatoma tenuis* (TL18-2, TL09-1, TL08-2), and *Stauroneis capitata* (TL18-2, TL09-1, TL08-2).

Although none of the records revealed a striking difference in the contribution of marine or brackish diatoms at depths corresponding to sand peaks, a slight increase in brackish diatoms (of up to 7%) was found for the sand peaks in TL09-1 and TL08-2 (27–28 and 27.5–28.5 cm, respectively; Fig. 4C and D). In TL18-2, sand peaks correlated to clear minima of *Achnanthidium petersenii* and *Platessa oblongella* (Fig. 7B), whereas the bottom peat clasts in TL27-1 and the sand layer in TL09-1 revealed noticeable maxima of *S. exiguiformis* (Fig. 7A, C). The distribution of the site scores on the PCA biplot for TL18-2 confirms the noticeable compositional difference between samples corresponding to sand peaks and majority of the remaining samples (Fig. 8). The first two axes of the PCA explained 37% of the variance, with PC1 being positively related primarily to *A. petersenii*. The biplot reveals that the site scores corresponding to the sand peaks are distinguished primarily by significantly negative PC1 values.

4.5. Characteristics of event layers in the peat pits

The litostratigraphy of peat pits along with their correlation with lake cores are presented in Fig. 9. The peat pits by TL27 lake (Fig. 2A) revealed numerous scattered pebbles and cobbles, as well as sand pockets ~7 cm below the surface in each of the three pits (Figs. 1B and 9).

The sediment characteristics in peat pits by Broad Pond varied from site to site. At the SE edge of the lake, in pit 18D, a 15-cm thick coarse sand layer containing well-rounded pebbles of different sizes (mostly <4 cm in diameter) was found ~10 cm below the surface (Figs. 2B and 9). In the nearby pits 18E and 18F, we found scattered, well-rounded pebbles and pockets of coarse sand within peat. At the SW edge of Broad Pond, in the most seaward (18A) and the most landward (18C) pits, only scattered pebbles were found approximately 15 and 8 cm below the surface, whereas pit 18B consisted of homogenous peat.

The peat pits by Porsh Pond and Frenchmans Pond revealed similar patterns (Fig. 2C and D). The most seaward locations at both sites (09A and 08A) contained a ~10 cm thick sand layer with pebbles ~10 cm below the surface (Fig. 9). In the more inland locations by each of the lakes, in pits 09B and 08B, sand layers were found at approximately the same depth. However, the layers were noticeably thinner with thicknesses of ~1 cm and ~5 cm in the sections next to the Porsh Pond and Frenchmans Pond, respectively. The most inland location by Porsh Pond, 09C, did not contain a sand layer, whereas by Frenchmans Pond in pit 08C the layer was ~1 cm thick.

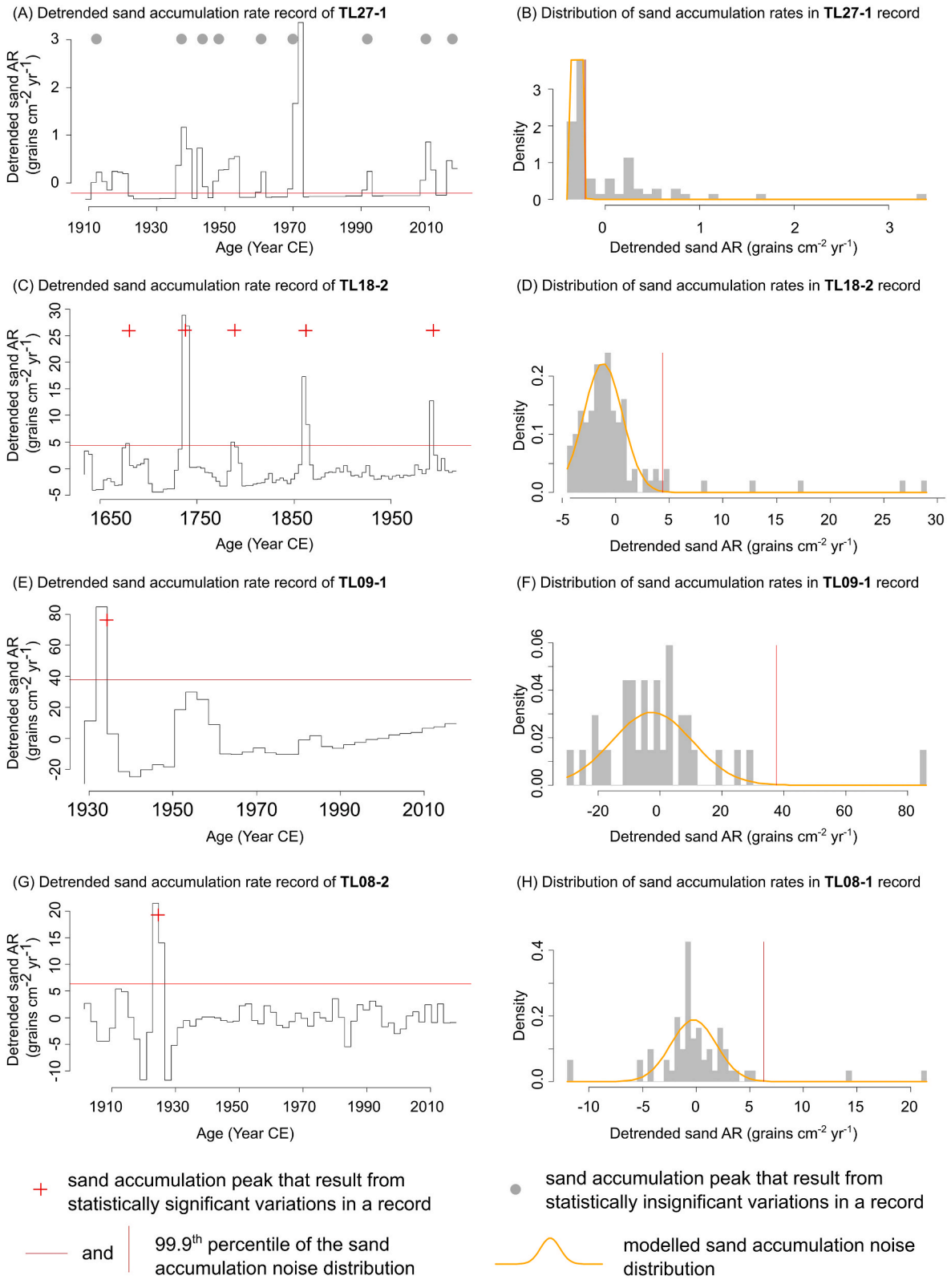

Fig. 6. Results of peak detection analysis performed for sand grain count records. (A, C, E, and G) Detrended sand accumulation rate records. The red horizontal lines show the threshold dividing observations into noise and peak components (values below and above the threshold, respectively). (B, D, F, H) Distribution of sand accumulation rates in the detrended series. The gray bars in the plots represent observed detrended sand accumulation rates, whereas the yellow lines show modeled Gaussian distributions of the noise components. The red vertical lines show the threshold dividing observations into noise and peak components (values below and above the threshold, respectively).

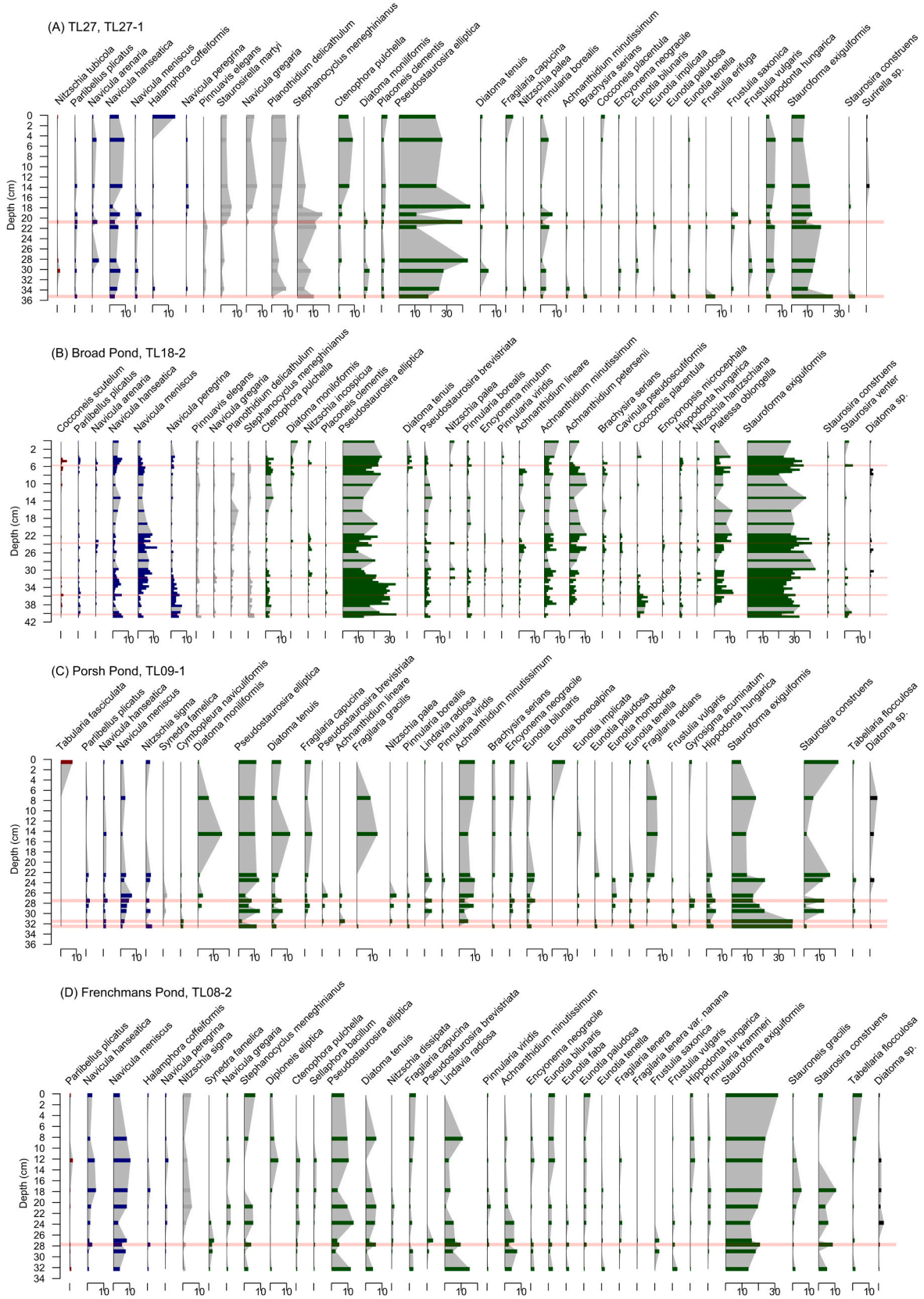

Fig. 7. Diatom compositions (% of the total counts) in the four investigated cores. Shown are 35 of the most abundant species for each of the cores grouped by their salinity preferences (red – marine; blue – brackish; gray – euryhaline; green – freshwater; black – undifferentiated). The translucent red bars mark the samples corresponding to the sedimentary event markers.

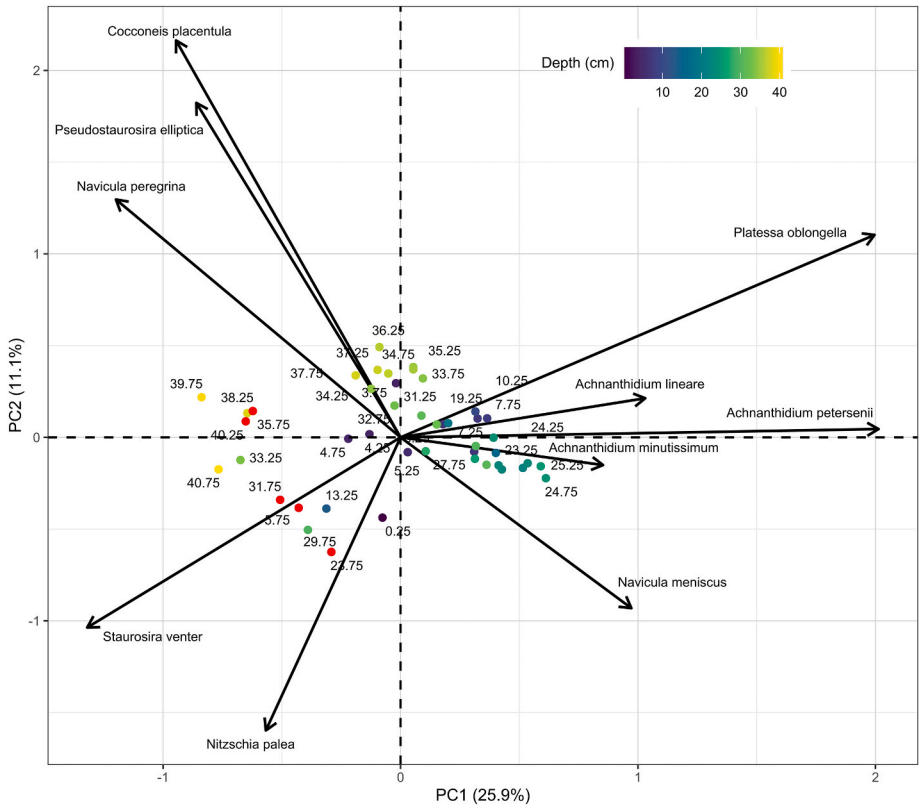

Fig. 8. Principal component analysis (PCA) biplots derived from the diatom data from TL18-2. Site scores are colored according to a corresponding core depth, except for samples associated with sand peaks, which are colored red. Variance explained by PC axes is provided in brackets.

4.6. Wave bases

The computed WB values ranged from 0.1 m for the average wind speed at Porsh Pond to 2.69 m at Broad Pond for a hurricane wind speed (extreme wind; Fig. 10). Although for each lake the differences in WB calculated for various wind directions were small and did not exceed 30 cm in the case of average wind speed, they were more pronounced for the extreme wind speed, reaching up to 1.61 m in the case of Frenchmans Pond (Fig. 10C). For TL27, the WB exceeded the coring depth for storm or extreme winds. At Frenchmans Pond, the WB exceeded the coring depth only under extreme winds from the southeast direction. For Broad Pond and Porsh Pond, the WB remained above the coring site's bottom regardless of wind direction, even if extreme wind is considered.

5. Discussion

5.1. Chronology

Although the studied lakes are shallow and possibly prone to bottom sediment mixing (Woszczyk et al., 2014) and ^{137}Cs remobilization (Foster et al., 2006), the cores revealed an overall exponential downcore decrease of $^{210}Pb_{ex}$ activity and in most cases clear ^{137}Cs peaks (Fig. 3). This suggests that no major disruption of sediment accumulation nor significant sediment mixing occurred. The latter observation aligns with the results of WB calculations, which suggest that wind-induced waves had no discernible impact on bottom sediments at coring locations in all lakes except TL27 (Fig. 10).

In TL27-1, the lack of a clear ^{137}Cs peak and lower r^2 for the exponential $^{210}Pb_{ex}$ fit curve (0.77; Fig. 3A) suggest some sediment mixing. This interpretation is supported by the WBs that exceed coring depth even in the case of winds blowing with the speed of a regular storm (Fig. 10). The reworking of sediments occurs despite the small lake area because the lake is very shallow (0.5 m). Stirring of the sediment by wind-induced water column mixing likely enhanced the internal loading of nutrients contributing to the high productivity of the lake indicated by the highest CFCS-derived MAR among the investigated lakes (0.04 g cm^{-2} yr^{-1}). The apparent reworking of sediment necessitates caution in the precise determination of the ages in this core.

In TL18-2, a clear ^{137}Cs peak and high r^2 for the exponential $^{210}Pb_{ex}$ fit curve (0.96, Fig. 3B) suggest that there was no significant sediment mixing. Selection of the age model does not substantially affect age estimates as all the models reveal similar deposition histories. The robustness of the age models is confirmed by their fit to the ^{137}Cs age markers. The age of sediment in the lower part of TL18-2 beyond the application limit of ^{210}Pb and ^{137}Cs can only be evaluated based on extrapolation, assuming stable MAR. Relatively stable LOI values in the upper 33 cm (~1770 CE onward) support this assumption. However, below ~33 cm, sediment composition changes noticeably as revealed by LOI and DBD profiles, indicating that MAR could have been different prior to ~1770 CE. Therefore, age estimates for the oldest part of the TL18-2 record should be treated with caution.

A high r^2 for the exponential $^{210}Pb_{ex}$ fit curve (0.94) in TL09-1 suggests mostly linear MARs that could have been occasionally disrupted by slight sediment reworking as indicated by the secondary ^{137}Cs peak found at 10–12 cm (Fig. 3C). Although all the models matched the NWT marker, the FF agreed only with the CRS piecewise model, and this model provides a date of 1929 CE for the bottom sand layer, consistent with the 1929 CE tsunami. The model also indicates a slightly higher MAR shortly after the tsunami.

For TL08-2, the r^2 is exceptionally high for the exponential $^{210}Pb_{ex}$ fit curve (0.98) and there is a clear ^{137}Cs peak (Fig. 3D), suggesting undisturbed, steady accumulation at the coring site that enables precise age estimations for the core. CIC and CRS models slightly deviate from FF and NWT markers. Moreover, CIC showed age reversals, whereas CRS revealed a "too-old" age error that is manifested in a noticeable shift toward older ages in the lowermost part of the profile (Binford, 1990).

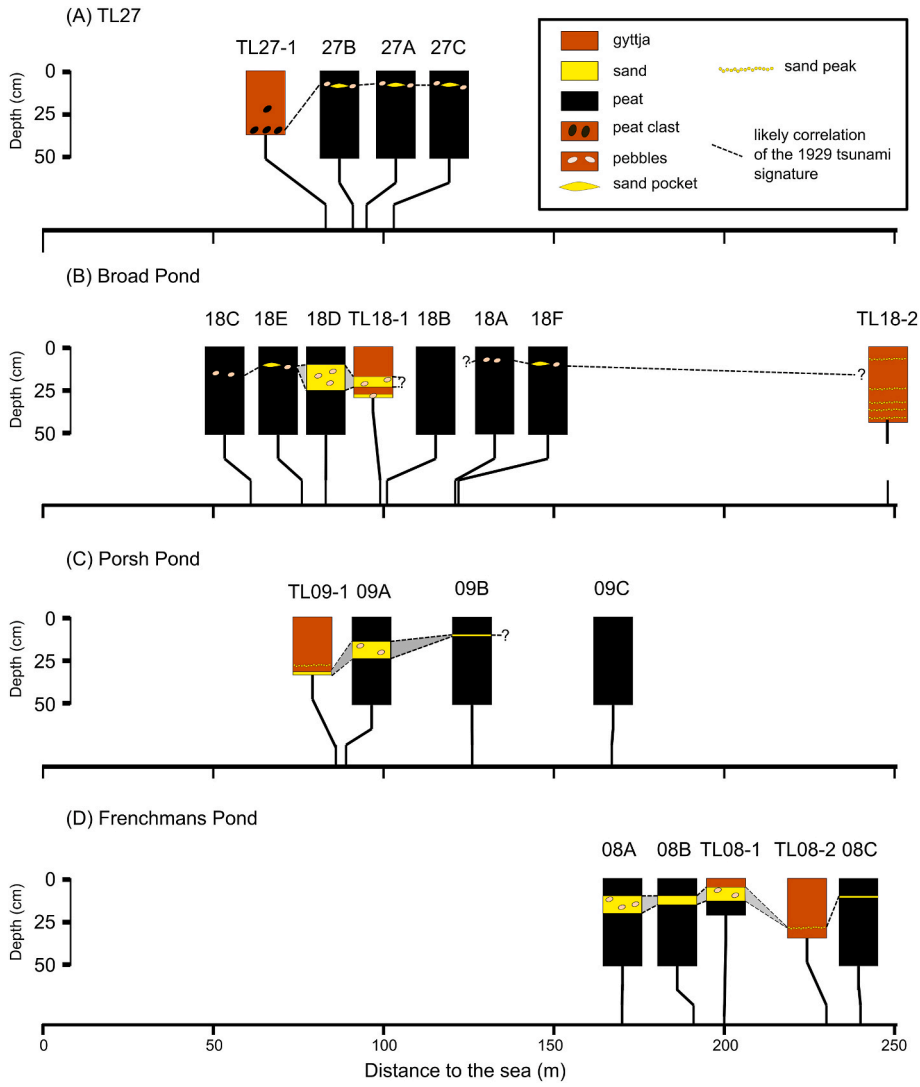

Fig. 9. Lithological profiles of the lake cores and peat pits arranged according to their distance from the sea. A likely lithostratigraphic correlation of the 1929 tsunami layers is shown.

Therefore, the CFCS model, which matched both FF and NWT markers, was used.

5.2. Identification of extreme coastal events

Records of extreme coastal events in lake sedimentary archives vary depending on the type and magnitude of an event, local settings (e.g., sediment sources, distance from the shoreline, bathymetry/topography), and sedimentary processes involved (e.g., Sabatier et al., 2022). The most-reported evidence of events, like tsunami or storm surges, includes erosional contacts, distinct sand layers, or macroscopically visible peat or lake mud clasts. Sometimes events may be recorded in the form of a small admixture of larger grains (e.g., Timmons et al., 2007) or different grain size distribution (e.g., Szcześniak et al., 2023). In the case of marine floods, the deposits are often characterized by marine indicators, e.g., microfossils, specific mineralogy, or geochemistry (e.g., Chagué-Goff et al., 2017; Goslin and Clemmensen, 2017; Kempf et al., 2015). Evidence of events can also be recognized in $^{210}Pb_{ex}$ profiles, as the event layers are often characterized by lower excess activities due to dilution of the $^{210}Pb_{ex}$ in a larger mass of sediments or input of older sediments (e.g., Arnaud et al., 2002). However, the identification and proper interpretation of the origin of these indicators must always consider the local context.

5.2.1. Sand layers

In our record, the single sand layers in cores TL18-1, TL09-1, and TL08-1 and several peat pits near the lakes, all located within c. 200 m from the seashore, most likely originated from the 1929 CE tsunami - the most catastrophic among the documented marine inundation events (Fig. 10). This interpretation is confirmed by the age-depth model of TL09-1 (Fig. 3C). Moreover, despite extensive surveys exploring peat deposits along the southern Burin Peninsula (Moore et al., 2007; Ruffman, 1996a; Tuttle et al., 2004), no other events have been confirmed to leave a thick sand layer in the area.

Although the records of TL27-1, TL18-2, and TL08-2 extend beyond 1929 CE, they do not contain visible sand layers corresponding to the tsunami (Fig. 4). In the case of TL27-1, the likely cause is a lack of potential sand source, while for TL18-2 and TL08-2, this might have resulted from the distant location of the coring sites in relation to the ocean coast (approximately 230 and 248 m, respectively) as clear sand layers were present in sediment cores collected closer to the seashore in both Broad Pond and Frenchmans Pond (TL18-1 and TL08-1; Fig. 5). More efficient sand deposition close to the seaward lake shores during tsunamis has been documented in other studies (Kempf et al., 2015; Sabatier et al., 2022). It can be explained by the rapid deceleration of tsunami flow upon reaching a water body and resulting fast sediment deposition.

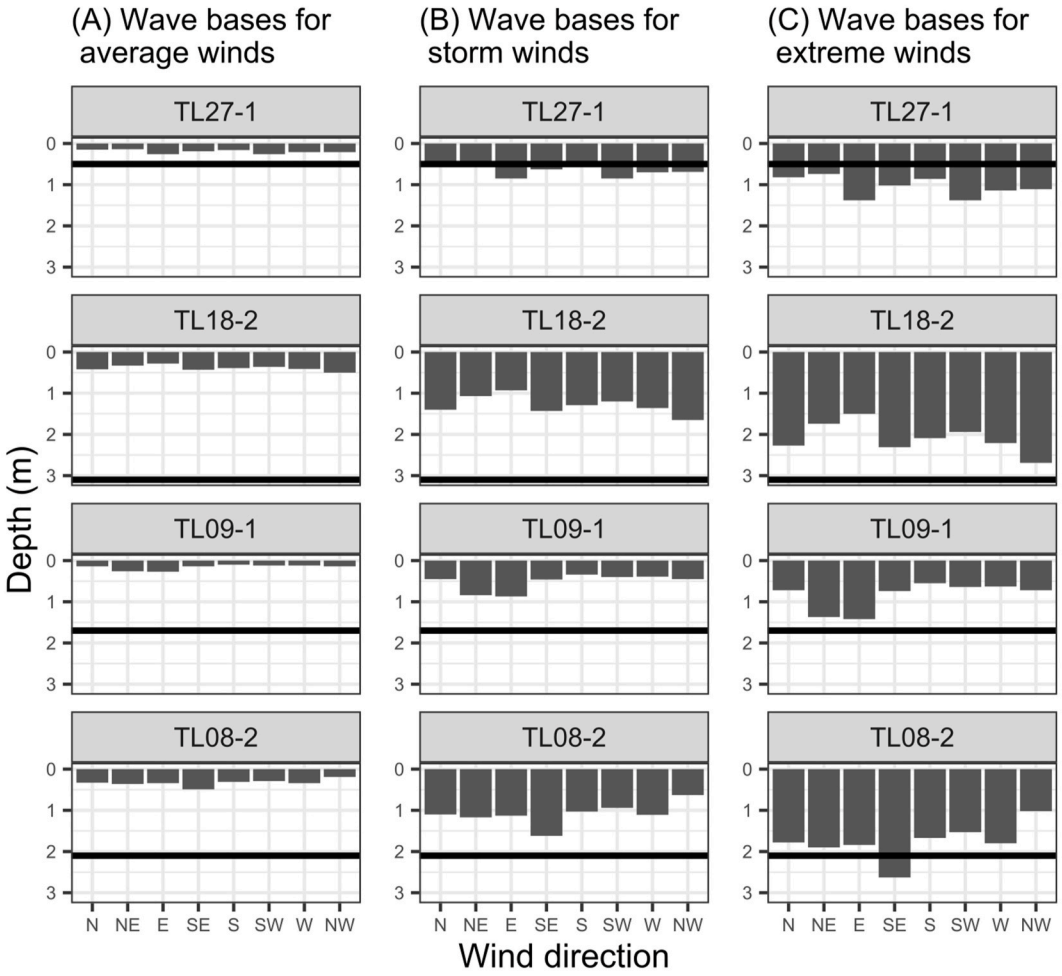

Fig. 10. Wind bases in the lakes in case of average (7.4 m s^{-1}; A), storm (28.6 m s^{-1}; B), and extreme (49.6 m s^{-1}; C) wind speeds. Black horizontal lines mark the coring depths. Wave bases exceeding the coring depths suggest resuspension of bottom sediments driven by wind-induced waves.

5.2.2. Peat clasts in lake sediments

We found eroded peat clasts only in core TL27-1, which was taken closest to the seashore (~70 m), and also close to the lake shores (~30 m; Fig. 10). The seashore next to the lake is sand-starved, mainly composed of cobbles (Fig. 2A), and the peat clasts are the only evidence of extreme events in this core. The peat clasts may come from the lake banks or adjacent peatland erosion. There are two size classes of clasts; the several cm in diameter peat clasts with the estimated age ranges of 1893–1928 CE in the deepest part of the core (Fig. 4A) and the smaller, several mm in diameter, clasts at 20–21 cm (~1962 CE). Taking into account the dating and historical data, the lower peat clast-rich layer most likely originated from the 1929 CE Grand Banks tsunami, as it was the largest high-magnitude event described for the study area, known to cause extensive erosion and deposition (Ruffman, 1996a; Tuttle et al., 2004). Deposition of peat clasts in coastal lakes was previously reported from other sites inundated by tsunamis (Bondevik et al., 1997; Kempf et al., 2015). The smaller peat clasts (20–21 cm) are not linked to any known historical event. So, they are likely related to smaller-scale ECE or anthropogenic activity.

5.2.3. Sand grain peaks

In coastal lakes, elevated sand content is often interpreted as a signature of an extreme aeolian event or increased storminess (Nielsen et al., 2016; Timmons et al., 2007). However, the direct wind transport of sand grains exceeding 0.25 mm in diameter (fraction counted in this study) to our coring locations appears unlikely, even during extreme wind speeds. Grains of this size are generally transported through saltation (Kok et al., 2012), with saltation distances increasing with wind speed. An experiment conducted by Liu et al. (2021) demonstrated that, under highly favorable conditions with wind speeds reaching 50 m s^{-1}, which exceed the maximum wind speeds recorded for the Burin Peninsula during Hurricane Michael, medium sand (0.25–0.50 mm) reaches a maximum saltation distance of approximately 9 m. This distance falls significantly short of the minimum distance to the coring site from the closest lake shoreline in our study (>22 m).

Given the frequent occurrence of winter storms in Newfoundland (Plante et al., 2015), it is advisable to account also for the impact of ice cover on lakes when assessing the sedimentary record. While specific data regarding ice-cover duration of the lakes is unavailable, the fact that on average temperatures are below 0 °C in January, February, and March (Climate Data, 2022) suggests that these lakes are at least occasionally frozen. A frozen lake surface serves as a suitable substrate for the saltation of sand grains, facilitating the accumulation of sediment related to extreme aeolian events directly onto the ice or snow (De Jong et al., 2007). Subsequently, particles that accumulate on the ice can be deposited into the lake when the ice melts, allowing for the recording of the event in the form of a sand peak.

Marine inundation (e.g., tsunami, storm flooding) is another type of event that can explain the presence of sand peaks in our records. These sand peaks can be attributed to the same processes elucidated in section 5.2.1, which describe the formation of sand layers. The eventual sedimentary record of a marine inundation event, either in the form of a sand peak or a sand layer depends on available sediment source and water flow depth and velocity, which generally decrease with distance

landward (e.g., Goto et al., 2012). Since the necessary source of sand is available in the coastal systems, and the coring sites are situated relatively close to the coastline (typically <250 m), we consider it likely that the sand peaks are associated with major marine inundations. In the case of an ice-covered lake, a distinct sedimentary signature of marine intrusion becomes even more plausible. The frozen surface allows for extended inundation and sediment transport, as the reduction in water velocity due to friction is smaller and may potentially lead to further inundation distance (Minoura et al., 1996).

Extreme precipitation events and resulting floods represent another potential contributor to event-like deposition of sand into lakes. However, our lakes are encompassed by extensive peatlands on the landward side, and the streams flowing into these lakes possess small catchment areas characterized by low relief and low sediment availability. Therefore, we consider it unlikely that extreme precipitation events account for our reported sand peaks.

Sand could have also been transported to the coring sites from the sandy-bottomed, shallower parts of the lake basins. Sediment instability and slumping exemplify a process capable of transporting sand from shallow to deeper regions of a lake basin. For instance, Pleskot et al. (2020) demonstrated that minor water level fluctuations could trigger sediment slumping leading to the deposition of several-centimeter-thick sandy gyttja layers in the deepest section of a relatively shallow lake (7 m). However, in the context of flat-bottom lakes like those investigated in this study, slumping alone is unlikely to assure transport of sand to the middle parts of the lakes due to the negligible inclination of the lake slopes. Calculated WB suggests sediment resuspension may potentially disturb sediment in shallower parts of the lakes (Fig. 10). If wind-induced resuspension occurs, subsequent sediment redistribution may be facilitated by wind-driven currents, which can attain speeds of several centimeters per second, even in relatively small coastal lakes if wind speed is considerable (Woszczyk et al., 2014). Consequently, we admit that sand peaks may result from sediment redistribution within lake basins, driven by extreme winds.

Extreme wind events and marine inundations appear to be the most plausible explanations for sand peaks. However, due to the potential involvement of multiple mechanisms in the formation of sand peaks in lake records, we refrain from attributing these peaks to any specific event type unless there is a clear historical association.

In TL08-2, a single statistically significant sand peak was reported, and it matches precisely the 1929 tsunami. Thus, the tsunami is the most likely cause for the presence of the peak. In TL09-1, above the tsunami sand layer, is a single statistically significant sand peak at 27–28 cm, dated to 1930–1946 CE (Fig. 4C). It should be noted that the timing of the event is shortly after the 1929 tsunami, thus, assuming erosion of the coast by the tsunami, the coastal barrier was likely in the initial phase of regeneration. Hence, if the peak is related to marine inundation, it did not have to be associated with particularly extreme water levels but instead was facilitated by less efficient protection of the lake from marine storms (Leszczyńska et al., 2022). The low magnitude of the event could explain its absence in the remaining lakes, including the nearby (~100 m away) Frenchmans Pond protected by relatively high dunes (Fig. 2D).

The TL18-2 core contains the longest record with the five statistically significant sand peaks (Fig. 4B). The age estimates for the sand peak at 5.5–6 cm (1989–1996 CE), at 23–24 (1849–1879 CE), and 40–40.5 cm (1657–1700 CE) are not correlated to any known events. However, sand peaks at 31.5–32 and 35–36 cm (1775–1806 and 1721–1771 CE), may correspond with the 1775 CE Great Independence Hurricane and the 1755 CE Lisbon tsunami. If this correlation holds true, it would be the first sedimentary evidence for the 1755 CE tsunami impact in the NW Atlantic (Costa et al., 2021) and the first-ever reported sedimentary trace of the 1775 CE hurricane. It is also the only core with no evidence of the 1929 CE tsunami. However, the core is the one located most landward and at the furthest distance from the shore of the lake, thus the transport capacity of the tsunami across the lake could be not sufficient.

5.2.4. Diatoms

Diatoms are widely used microfossils in studies of ECE (e.g., Dura and Hemphill-Haley, 2020). However, the diatom signature of event deposits in coastal lakes and coastal plains may exhibit considerable variability. These deposits may comprise a mixed assemblage, with marine taxa predominating (e.g., Dura et al., 2016; Kokociński et al., 2009), a minor admixture of marine or brackish diatoms (e.g., Long et al., 2015), or even be entirely dominated by non-marine species (e.g., Szczuciński et al., 2012). In this study, samples corresponding to a sand layer, sand peaks, and peat clasts did not exhibit large differences in diatom composition compared to adjacent samples. However, subtle changes were observed, which may supplement the identification of ECE. These changes include an elevated contribution of *Stauroforma exiguiformis*, a decline of some freshwater species, and a slight increase in the abundance of brackish diatoms.

The sediment samples assigned to the 1929 CE tsunami in cores TL09-1 and TL27-1 exhibited particularly high contributions of *S. exiguiformis* (Fig. 7A, C), while the increase in TL08-2 is less evident (Fig. 7D). As the species commonly thrives in coastal freshwater-to-slightly-brackish environments, its high percentages can be attributed to sediment erosion in the vicinity of the lakes caused by the tsunami. However, utility of this taxon as a singular indicator for marine incursions is limited, given its consistently high relative abundance in all sediment cores.

In TL18-2, a high-resolution diatom analysis revealed a discernible decline in two freshwater species, namely *Platessa oblongella* and *Achnanthidium petersenii*, at the depths corresponding to the sand peaks (Fig. 7B). While the changes in diatom assemblages within the samples from the event horizons were not dramatic, their distinct composition was confirmed by their clustering in the PCA ordination space (Fig. 8). However, it is important to note that the magnitude of this change is relatively subtle, and as such, it does not provide unequivocal evidence for a marine inundation.

The sediment characterized by sand peaks observed in cores TL09-1 and TL08-2 exhibits a slight increase in the contribution of brackish taxa (Fig. 4C and D). While this change supports our assumption associating these peaks with marine inundation events, it is essential to note that the shift in diatom composition is very subtle.

The relatively minor changes in diatom composition observed across all the lakes are likely attributable to two primary factors. Firstly, these lakes harbor diatom communities that have likely adapted to elevated salinity levels, rendering them resilient to marine water incursions. This assumption is in line with the continuous presence and relatively high abundance of brackish diatoms in all the records. The second reason for the limited turnover in diatom composition at the event horizons is linked to the timing of some ECEs. It remains likely that marine intrusions occurring during the cold season when diatom abundance in the sea experiences a seasonal low, may limit the influx of halophilic species into the lakes.

5.3. History of ECE in the southern Burin Peninsula

Our lake sediment records contain evidence for three known major historical ECEs (Fig. 11), namely the 1755 CE Lisbon tsunami (TL18-2), the 1775 CE Great Independence Hurricane (TL18-2), and the 1929 CE Newfoundland tsunami (TL27-1, TL09-1, and TL08-2). While none of the sedimentary event markers precisely match the 1983 and 2000 CE winter storms, there remains a plausible association of the sand peak from TL18-2, dated to 1989–1999 CE, with one of these events (Fig. 10). Moreover, our findings suggest the occurrence of four undocumented ECE events: 1657–1700 CE (TL18-2), 1849–1879 CE (TL18-2), 1930–1946 CE (TL09-1), and 1952–1973 CE (TL27-1). In total, at least eight ECEs have been recorded on the southern Burin Peninsula within the last approximately 350 years, with most events likely being associated with marine inundations or possibly extreme wind events. Consequently, a mean ECEs recurrence interval can be roughly calculated to

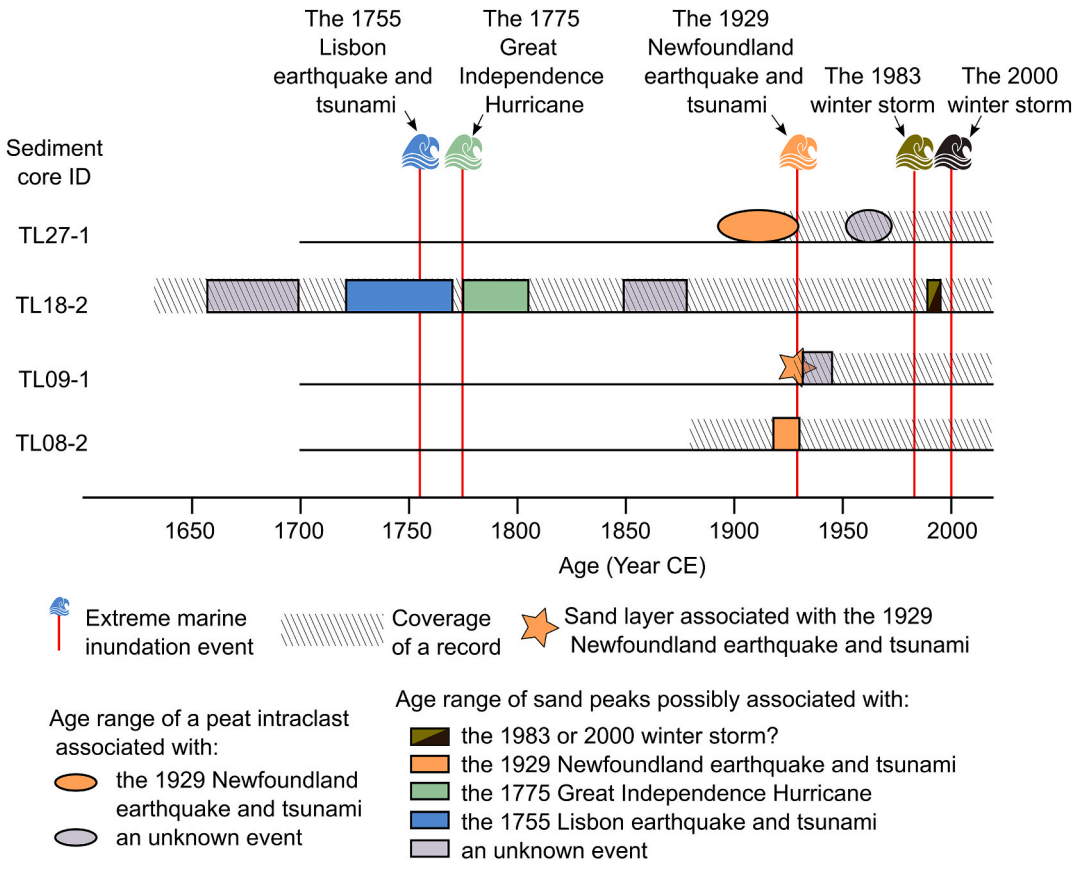

Fig. 11. Summary figure combining sedimentary records of extreme coastal events with the historical data.

be in the order of 40 years, or c. 55 years if we consider only non-tsunami events. This roughly matches the interval of 10–50 years for major marine inundation events in Newfoundland estimated by Forbes (1984).

Three of six non-tsunami ECEs documented in our record occurred during the 20th century, hinting at a potential shift towards a regime with higher event frequency in the relatively recent past. However, it is crucial to acknowledge that only one sediment core covered the pre-20th century period. Nevertheless, our supposition finds additional support from the paleo-storm study by Patterson et al. (2022). Their investigation of a 520-year-long lake sediment record from south-western New Brunswick (~900 km to SW from the Burin Peninsula) revealed an exceptionally high frequency of tropical cyclones during the 20th century.

Reconstructing the magnitude of past ECEs often relies on the distinctiveness of their sedimentary imprints (Goslin and Clemmensen, 2017). However, the deposition of sediments in coastal lakes during coastal flooding is influenced by various factors independent of the event magnitude. These factors include sediment availability, coastal settings at the time of the event, and the pattern of sediment redistribution within a lake basin. Consequently, caution must be exercised when attempting to reconstruct the relative magnitude of an event from coastal lake sediments (Sabatier et al., 2022). Nonetheless, the extensive sedimentary evidence of the 1929 CE tsunami in our records provides substantial support for its exceptionally high magnitude (Ruffman, 1996b; Tuttle et al., 2004). In contrast, all the younger ECEs exhibit less distinct sedimentary traces and lack replication in multiple cores, suggesting that their impacts were more localized. Evaluating the magnitude of events predating the 1929 CE tsunami poses particular challenges, as it relies primarily on TL18-2, the core without a clear signal of the 1929 CE tsunami. It is worth noting the presence of an exceptionally distinct sand peak accompanied by pebbles at 35–36 cm in this core. If our correlation of this peak with the 1755 CE tsunami is accurate, then the threats from far-field tsunamis need to be taken seriously in hazard assessment for Canada's east coast (Roger et al., 2010).

6. Conclusions

We present eastern Canada's northernmost lake-sediment-based reconstruction of the extreme coastal event history. The results lead to several conclusions and challenges for future research, in particular:

1. Lake sediment records have proven valuable for reconstructing event histories. However, no single site recorded all the events, and no single event was found at all sites, highlighting the importance of using both extensive and intensive sampling approach involving multiple sediment cores from a number of lakes, and analyzing them using a multiproxy approach and a good understanding of local context. Only such an approach can produce comprehensive reconstructions needed for proper coastal hazard assessment.
2. The mean recurrence interval of major weather-related events (e.g., hurricanes) was estimated to be approximately 55 years, with a possible increase in event frequency during the last century. A better understanding of the potential links between event frequency and climate would greatly benefit from multisite, well-dated records.
3. The 1929 CE tsunami was likely the most catastrophic ECE in the area. However, the event marker likely corresponding to the 1755 CE Lisbon tsunami suggests its impacts could also have been substantial, highlighting the need to take far-field tsunami hazards in Newfoundland seriously. However, the lack of evidence of this event in earlier studies on coastal plains calls for the need to confirm this finding.

4. Although diatoms did not provide unequivocal evidence of ECEs, they revealed subtle changes associated with them. However, better insights into the character and significance of the reported shifts in species compositions would require a much better understanding of the local drivers of changes in diatom communities.

CRediT authorship contribution statement

Krzysztof Pleskot: Conceptualization, Data curation, Funding acquisition, Investigation, Visualization, Writing – original draft. **Les C. Cwynar:** Conceptualization, Funding acquisition, Supervision, Writing – review & editing. **Cyprian Kowalczyk:** Investigation, Writing – review & editing. **Mikołaj Kokociński:** Investigation, Writing – review & editing. **Witold Szczuciński:** Conceptualization, Investigation, Supervision, Writing – review & editing.

Declaration of competing interest

The authors declare that they have no known competing financial interests or personal relationships that could have appeared to influence the work reported in this paper.

Data availability

Data and code to reproduce the analyses are available at https://github.com/krzypl/ms_refininig_history_of_ece.git

Acknowledgments

Two anonymous reviewers are thanked for their thoughtful suggestions that markedly improved the quality of this work. The study was financed through a grant from the Polish National Science Centre (NCN), grant no. 2020/37/B/ST10/02614, and a Discovery Grant to L. C. Cwynar from the Natural Sciences and Engineering Research Council of Canada. We would like to express our gratitude to Patricia Nancekivell for her invaluable help during the fieldwork.

References

Appleby, P., 2001. Chronostratigraphic techniques in recent sediments. In: Last, W.M., Smol, J.P. (Eds.), Tracking Environmental Change Using Lake Sediments: Basin Analysis, Coring, and Chronological Techniques. Springer, Dordrecht, pp. 171–203.

Appleby, P.G., Oldfield, F., 1978. The calculation of lead-210 dates assuming a constant rate of supply of unsupported ^{210}Pb to the sediment. Catena 5, 1–8. https://doi.org/10.1016/S0341-8162(78)80002-2.

Arnaud, F., Lignier, V., Revel, M., Desmet, M., Beck, C., Pourchet, M., Charlet, F., Trentesaux, A., Tribovillard, N., 2002. Flood and earthquake disturbance of ^{210}Pb geochronology (lake anterne, NW alps). Terra. Nova 14, 225–232. https://doi.org/10.1046/j.1365-3121.2002.00413.x.

Bąk, A., Witkowski, A., Żelazna-Wieczorek, J., Wojtal, A.Z., Szczepocka, E., Szulc, K., Szulc, Z., 2012. Klucz do oznaczania okrzemek w fitobentosie na potrzeby oceny stanu ekologicznego wód powierzchniowych w Polsce. Biblioteka Monitoringu Środowiska, Warsaw (in Polish).

Barkan, R., ten Brink, U.S., Lin, J., 2009. Far field tsunami simulations of the 1755 Lisbon earthquake: implications for tsunami hazard to the U.S. East Coast and the Caribbean. Mar. Geol. 264, 109–122. https://doi.org/10.1016/j.margeo.2008.10.010.

Battarbee, R.W., 1986. Diatom analysis. In: Berglund, B. (Ed.), Handbook of Holocene Palaeoecology and Palaeohydrology. John Wiley & Sons, Chichester, pp. 527–570.

Batterson, M.J., Liverman, D.G.E., Taylor, D., Ryan, J., 1999. The Assessment of Geological Hazards in Newfoundland—an Update (No. 99–1), Current Research, Newfoundland Department of Mines and Energy. Geological Survey Branch.

Besonen, M.R., Bradley, R.S., Mudelsee, M., Abbott, M.B., Francus, P., 2008. A 1,000-year, annually-resolved record of hurricane activity from Boston, Massachusetts. Geophys. Res. Lett. 35, L14705 https://doi.org/10.1029/2008GL033950.

Binford, M.W., 1990. Calculation and uncertainty analysis of ^{210}Pb dates for PIRLA project lake sediment cores. J. Paleolimnol. 3, 253–267. https://doi.org/10.1007/BF00219461.

Bondevik, S., Inge Svendsen, J., Mangerud, J., 1997. Tsunami sedimentary facies deposited by the Storegga tsunami in shallow marine basins and coastal lakes, western Norway. Sedimentology 44, 1115–1131. https://doi.org/10.1046/j.1365-3091.1997.d01-63.x.

Bowyer, P., 2014. Canadian Tropical Cyclone Season Summary for 2000 [WWW Document]. URL. https://www.ec.gc.ca/ouragans-hurricanes/default.asp?lang=en&n=9805D6F1-1, 9.11.23.

Bruel, R., Sabatier, P., 2020. serac: an R package for ShortlivEd RAdionuclide chronology of recent sediment cores. J. Environ. Radioact. 225, 106449 https://doi.org/10.1016/j.jenvrad.2020.106449.

Canadian Hydrographic Service, 2022. Tide and Current Tables [WWW Document]. URL. https://www.tides.gc.ca/tides/en/stations/00755, 7.30.22.

Chagué-Goff, C., Szczuciński, W., Shinozaki, T., 2017. Applications of geochemistry in tsunami research: a review. Earth Sci. Rev. 165, 203–244. https://doi.org/10.1016/j.earscirev.2016.12.003.

Climate Data, 2022. Lamaline Climate: Average Temperature weather by month [WWW Document]. URL. https://en.climate-data.org/ameryka-po%C5%82nocna/kanada/newfoundland-and-labrador/lamaline-57462/, 7.30.22.

Cochard, R., Ranamukhaarachchi, S.L., Shivakoti, G.P., Shipin, O.V., Edwards, P.J., Seeland, K.T., 2008. The 2004 tsunami in Aceh and Southern Thailand: a review on coastal ecosystems, wave hazards and vulnerability. Perspect. Plant Ecol. Evol. Systemat. 10, 3–40. https://doi.org/10.1016/j.ppees.2007.11.001.

Costa, P.J.M., Dawson, S., Ramalho, R.S., Engel, M., Dourado, F., Bosnic, I., Andrade, C., 2021. A review on onshore tsunami deposits along the Atlantic coasts. Earth Sci. Rev. 212, 103441 https://doi.org/10.1016/j.earscirev.2020.103441.

Damman, A.W., 1983. An ecological subdivision of the island of Newfoundland. In: Biogeography and Ecology of the Island of Newfoundland. Springer Science & Business Media, pp. 163–206.

Danard, M., Munro, A., Murty, T., 2003. Storm surge hazard in Canada. Nat. Hazards 28, 407–431. https://doi.org/10.1023/A:1022990310410.

Das, O., Wang, Y., Donoghue, J., Xu, X., Coor, J., Elsner, J., Xu, Y., 2013. Reconstruction of paleostorms and paleoenvironment using geochemical proxies archived in the sediments of two coastal lakes in northwest Florida. Quat. Sci. Rev. 68, 142–153. https://doi.org/10.1016/j.quascirev.2013.02.014.

Davis, N.N., Badger, J., Hahmann, A.N., Hansen, B.O., Mortensen, N.G., Kelly, M., Larsén, X.G., Olsen, B.T., Floors, R., Lizcano, G., Casso, P., Lacave, O., Bosch, A., Bauwens, I., Knight, O.J., Potter Van Loon, A., Fox, R., Parvanyan, T., Krohn Hansen, S.B., Heathfield, D., Onninen, M., Drummond, R., 2023. The global wind Atlas: a high-resolution dataset of climatologies and associated web-based application. Bull. Am. Meteorol. Soc. 104, E1507–E1525. https://doi.org/10.1175/BAMS-D-21-0075.1.

De Jong, R., Schoning, K., Björck, S., 2007. Increased aeolian activity during humidity shifts as recorded in a raised bog in south-west Sweden during the past 1700 years. Clim. Past 3, 411–422. https://doi.org/10.5194/cp-3-411-2007.

Donnelly, J.P., Butler, J., Roll, S., Wengren, M., Webb III, T., 2004. A backbarrier overwash record of intense storms from Brigantine, New Jersey. Mar. Geol. 210, 107–121. https://doi.org/10.1016/j.margeo.2004.05.005.

Dunnington, D.W., Libera, N., Kurek, J., Spooner, I.S., Gagnon, G.A., 2022. Tidypaleo : visualizing paleoenvironmental archives using ggplot2. J. Stat. Software 101. https://doi.org/10.18637/jss.v101.i07.

Dura, T., Hemphill-Haley, E., 2020. Diatoms in tsunami deposits. In: Geological Records of Tsunamis and Other Extreme Waves. Elsevier, pp. 291–322. https://doi.org/10.1016/B978-0-12-815686-5.00014-6.

Dura, T., Hemphill-Haley, E., Sawai, Y., Horton, B.P., 2016. The application of diatoms to reconstruct the history of subduction zone earthquakes and tsunamis. Earth Sci. Rev. 152, 181–197. https://doi.org/10.1016/j.earscirev.2015.11.017.

Engel, M., Pilarczyk, J., May, S.M., Brill, D., Garrett, E., 2020a. Geological Records of Tsunamis and Other Extreme Waves. Elsevier.

Engel, M., Schön, I., Patel, T., Pawłowski, J., Szczuciński, W., Dawson, S., Garrett, E., Heyvaert, V.M., 2020b. Paleogenetic approaches in tsunami deposit studies. In: Engel, M., Pilarczyk, J., May, S.M., Brill, D., Garrett, E. (Eds.), Geological Records of Tsunamis and Other Extreme Waves. Elsevier, pp. 427–442.

Finsinger, W., Bonnici, I., 2022. Tapas: an R Package to Perform Trend and Peaks Analysis. Zenodo. https://doi.org/10.5281/zenodo.6344463.

Forbes, D., 1984. Coastal geomorphology and sediments of Newfoundland. In: Current Research, Part B, Geol. Surv. Can., 84–1B, pp. 11–24.

Foster, I.D.L., Mighall, T.M., Proffitt, H., Walling, D.E., Owens, P.N., 2006. Post-depositional ^{137}Cs mobility in the sediments of three shallow coastal lagoons, SW england. J. Paleolimnol. 35, 881–895. https://doi.org/10.1007/s10933-005-6187-6.

Glew, J.R., 1991. Miniature gravity corer for recovering short sediment cores. J. Paleolimnol. 5, 285–287. https://doi.org/10.1007/BF00200351.

Goslin, J., Clemmensen, L.B., 2017. Proxy records of Holocene storm events in coastal barrier systems: storm-wave induced markers. Quat. Sci. Rev. 174, 80–119. https://doi.org/10.1016/j.quascirev.2017.08.026.

Goto, K., Ishizawa, T., Ebina, Y., Imamura, F., Sato, S., Udo, K., 2021. Ten years after the 2011 Tohoku-oki earthquake and tsunami: geological and environmental effects and implications for disaster policy changes. Earth Sci. Rev. 212, 103417 https://doi.org/10.1016/j.earscirev.2020.103417.

Goto, K., Sugawara, D., Ikema, S., Miyagi, T., 2012. Sedimentary processes associated with sand and boulder deposits formed by the 2011 Tohoku-oki tsunami at Sabusawa Island. Japan. Sediment. Geol. 282, 188–198. https://doi.org/10.1016/j.sedgeo.2012.03.017.

Guiry, M.D., Guiry, G.M., 2023. AlgaeBase [WWW Document]. World-Wide Electron. Publ. Natl. Univ. Irel. Galway. URL. https://www.algaebase.org.

Heiri, O., Lotter, A.F., Lemcke, G., 2001. Loss on ignition as a method for estimating organic and carbonate content in sediments: reproducibility and comparability of results. J. Paleolimnol. 25, 101–110. https://doi.org/10.1023/A:1008119611481.

Hickman, H., 2006. Flood Hazard and Vulnerability in Newfoundland Communities. (Master Thesis). Memorial University of Newfoundland. https://research.library.mun.ca/10651/.

Higuera, P.E., Gavin, D.G., Bartlein, P.J., Hallett, D.J., 2010. Peak detection in sediment - charcoal records: impacts of alternative data analysis methods on fire-history interpretations. Int. J. Wildland Fire 19, 996–1014. https://doi.org/10.1071/WF09134.

Juggins, S., 2020. Rioja: Analysis of Quaternary Science Data. R package version 0.9-26. https://cran.r-project.org/package=rioja.

Kelsey, H.M., Nelson, A.R., Hemphill-Haley, E., Witter, R.C., 2005. Tsunami history of an Oregon coastal lake reveals a 4600 yr record of great earthquakes on the Cascadia subduction zone. Geol. Soc. Am. Bull. 117, 1009–1032. https://doi.org/10.1130/b25452.1.

Kemp, A.C., Wright, A.J., Edwards, R.J., Barnett, R.L., Brain, M.J., Kopp, R.E., Cahill, N., Horton, B.P., Charman, D.J., Hawkes, A.D., Hill, T.D., van de Plassche, O., 2018. Relative sea-level change in Newfoundland, Canada during the past ~3000 years. Quat. Sci. Rev. 201, 89–110. https://doi.org/10.1016/j.quascirev.2018.10.012.

Kempf, P., Moernaut, J., Van Daele, M., Vermassen, F., Vandoorne, W., Pino, M., Urrutía, R., Schmidt, S., Garrett, E., De Batist, M., 2015. The sedimentary record of the 1960 tsunami in two coastal lakes on Isla de Chiloé, south central Chile. Sediment. Geol. 328, 73–86. https://doi.org/10.1016/j.sedgeo.2015.08.004.

Kok, J.F., Parteli, E.J.R., Michaels, T.I., Karam, D.B., 2012. The physics of wind-blown sand and dust. Rep. Prog. Phys. 75, 106901 https://doi.org/10.1088/0034-4885/75/10/106901.

Kokociński, M., Szczuciński, W., Zgrundo, A., Ibragimow, A., 2009. Diatom assemblages in 26 December 2004 tsunami deposits from coastal zone of Thailand as sediment provenance indicators. Pol. J. Environ. Stud. 18, 93–101.

Krammer, K., Lange-Bertalot, H., 1991. Bacillariophyceae: achnanthaceae, Kritische Ergänzungen zu *Navicula* (Lineolatae) und *Gomphonema* Gesamtliterarurverzeichnis. In: Ettl, H., Gerloff, J., Heynig, H., Mollenhauer, D. (Eds.), Süsswasserflora von Mitteleuropa. Bd. 2, Teil. 4. Gustav Fischer, Stuttgart, p. 437.

Krishnaswamy, S., Lal, D., Martin, J.M., Meybeck, M., 1971. Geochronology of lake sediments. Earth Planet Sci. Lett. 11, 407–414. https://doi.org/10.1016/0012-821X(71)90202-0.

Leszczyńska, K., Stattegger, K., Moskalewicz, D., Jagodziński, R., Kokociński, M., Niedzielski, P., Szczuciński, W., 2022. Controls on coastal flooding in the southern Baltic Sea. Sci. Rep. 12, 9710. https://doi.org/10.1038/s41598-022-13860-4.

Liu, B., Wang, Z., Niu, B., Qu, J., 2021. Large scale sand saltation over hard surface: a controlled experiment in still air. J. Arid Land 13, 599–611. https://doi.org/10.1007/s40333-021-0104-3.

Liverman, D., Batterson, M., Taylor, D., Ryan, J., 2001. Geological hazards and disasters in Newfoundland and labrador. Can. Geotech. J. 38, 936–956. https://doi.org/10.1139/t01-022.

Long, A.J., Szczuciński, W., Lawrence, T., 2015. Sedimentary evidence for a mid-Holocene iceberg-generated tsunami in a coastal lake, west Greenland. arktos 1, 6. https://doi.org/10.1007/s41063-015-0007-7.

Løvholt, F., Schulten, I., Mosher, D., Harbitz, C., Krastel, S., 2019. Modelling the 1929 Grand Banks slump and landslide tsunami. Geol. Soc. Lond. Spec. Publ. 477, 315–331. https://doi.org/10.1144/SP477.28.

Minoura, K., Gusiakov, V., Kurbatov, A., Takeuti, S., Svendsen, J., Bondevik, S., Oda, T., 1996. Tsunami sedimentation associated with the 1923 Kamchatka earthquake. Sediment. Geol. 106, 145–154. https://doi.org/10.1016/0037-0738(95)00148.

Moore, A.L., McAdoo, B.G., Ruffman, A., 2007. Landward fining from multiple sources in a sand sheet deposited by the 1929 Grand Banks tsunami. Newfoundland. Sediment. Geol. 200, 336–346. https://doi.org/10.1016/j.sedgeo.2007.01.012.

Murty, T.S., Greenberg, D.A., 1987. Numerical simulation of the storm surge of January 1982 on the south coast of Newfoundland. Atmos.-Ocean 25, 46–59. https://doi.org/10.1080/07055900.1987.9649263.

Murty, T.S., Venkatesh, S., Danard, M.B., El-Sabh, M.I., 1995. Storm surges in Canadian waters. Atmos.-Ocean 33, 359–387. https://doi.org/10.1080/07055900.1995.9649537.

Neu, H.J.A., 1982. 11-year Deep-Water Wave Climate of Canadian Atlantic Waters (No. 13). Canadian Technical Report of Hydrography and Ocean Sceinces, Dartmouth.

Nielsen, P.R., Dahl, S.O., Jansen, H.L., 2016. Mid- to late Holocene aeolian activity recorded in a coastal dunefield and lacustrine sediments on Andøya, northern Norway. Holocene 26, 1486–1501. https://doi.org/10.1177/0959683616640050.

NOAA, 2023. Estimating Wind Speeds with Visual Clues [WWW Document]. URL. https://www.weather.gov/pqr/wind.

Oksanen, J., Simpson, G.L., Blanchet, F.G., Kindt, R., Legendre, P., Minchin, P.R., O'Hara, R.B., Solymos, P., Stevens, M.H.H., Szoecs, E., Wagner, H., Barbour, M., Bedward, M., Bolker, B., Borcard, D., Carvalho, G., Chirico, M., Caceres, M.D., Durand, S., Evangelista, H.B.A., FitzJohn, R., Friendly, M., Furneaux, B., Hannigan, G., Hill, M.O., Lahti, L., McGlinn, D., Ouellette, M.-H., Cunha, E.R., Smith, T., Stier, A., Braak, C.J.F.T., Weedon, J., 2022. vegan: Community Ecology Package. R package version 2.6-2. https://CRAN.R-project.org/package=vegan.

Oliva, F., Viau, A.E., Peros, M.C., Bouchard, M., 2018. Paleotempestology database for the western North Atlantic basin. Holocene 28, 1664–1671. https://doi.org/10.1177/0959683618782598.

Orme, L.C., Reinhardt, L., Jones, R.T., Charman, D.J., Barkwith, A., Ellis, M.A., 2016. Aeolian sediment reconstructions from the Scottish Outer Hebrides: Late Holocene storminess and the role of the North Atlantic Oscillation. Quat. Sci. Rev. 132, 15–25. https://doi.org/10.1016/j.quascirev.2015.10.045.

Patterson, R.T., Mazzella, V., Macumber, A.L., Gregory, B.R.B., Patterson, C.W., Nasser, N.A., Roe, H.M., Galloway, J.M., Reinhardt, E.G., 2020. A novel protocol for mapping the spatial distribution of storm derived sediment in lakes. SN Appl. Sci. 2, 2125. https://doi.org/10.1007/s42452-020-03908-3.

Patterson, R.T., Nasser, N.A., Reinhardt, E.G., Patterson, C.W., Gregory, B.R.B., Mazzella, V., Roe, H.M., Galloway, J.M., 2022. End-member mixing analysis as a tool for the detection of major storms in lake sediment records. Paleoceanogr. Paleoclimatol. 37 https://doi.org/10.1029/2022PA004510 e2022PA004510.

Pennington, W., Tutin, T.G., Cambray, R.S., Fisher, E.M., 1973. Observations on lake sediments using fallout ^{137}Cs as a tracer. Nature 242, 324–326. https://doi.org/10.1038/242324a0.

Plante, M., Son, S.-W., Atallah, E., Gyakum, J., Grise, K., 2015. Extratropical cyclone climatology across eastern Canada. Int. J. Climatol. 35, 2759–2776. https://doi.org/10.1002/joc.4170.

Pleskot, K., Apolinarska, K., Kołaczek, P., Suchora, M., Fojutowski, M., Joniak, T., Kotrys, B., Kramkowski, M., Słowiński, M., Woźniak, M., Lamentowicz, M., 2020. Searching for the 4.2 ka climate event at Lake Spore, Poland. Catena 191, 104565. https://doi.org/10.1016/j.catena.2020.104565.

R Core Team, 2022. R: A Language and Environment for Statistical Computing. R Foundation for Statistical Computing, Vienna, Austria.

Reichardt, E., 1999. Zur Revision der Gattung Gomphonema. Die Arten um G. Affine/Insigne, G. angustum/micropus, G. acuminatum sowie gomphonemoide Diatomeen aus dem Oberoligozän in Böhmen. In: Lange-Bertalot, H. (Ed.), Iconographia Diatomologica Volume 8 Taxonomy. A.R.G. Ganter Verlag K.G. . Koeltz Scientific Books, Ruggell, p. 203.

Robbins, J.A., 1978. Geochemical and geophysical applications of radioactive lead. In: Biogeochemistry of Lead in the Environment. Elsevier Scientific, Amsterdam, pp. 285–393.

Roger, J., Baptista, M.A., Mosher, D., Hébert, H., Sahal, A., 2010. Tsunami impact on Newfoundland, Canada, due to far-field generated tsunamis. Implications on hazard assessment. In: Proc. 9th US Natl. 10th Can. Conf. Earthq. Eng., pp. 25–29.

Ruffman, A., 1996a. Tsunami Runup Mapping as an Emergency Preparedness Planning Tool: the 1929 Tsunami in St. Lawrence. Newfoundland. Emergency Preparedness Canada, Ottawa.

Ruffman, A., 1996b. The multidisciplinary rediscovery and tracking of "The Great Newfoundland and Saint-Pierre et Miquelon Hurricane of September 1775". North. Mar. 6, 11–23.

Sabatier, P., Moernaut, J., Bertrand, S., Van Daele, M., Kremer, K., Chaumillon, E., Arnaud, F., 2022. A review of event deposits in lake sediments. Quaternary 5, 34. https://doi.org/10.3390/quat5030034.

Simpson, G.L., 2019. Ggvegan: "Ggplot2" Plots for the "Vegan" Package. R Package Version 0.1-0.

Smith, I., Sinclair, I., 1972. Deep water waves in lakes. Freshw. Biol. 2, 387–399.

Szcześniak, M., Kokociński, M., Jagodziński, R., Pleskot, K., Zajączkowski, M., Szczuciński, W., 2023. Late Holocene Vistula River floods recorded in grain size distributions and diatom assemblages of marine sediments of the Gulf of Gdańsk (Baltic Sea). Palaeogeogr. Palaeoclimatol. Palaeoecol. 617, 111499 https://doi.org/10.1016/j.palaeo.2023.111499.

Szczuciński, W., Kokociński, M., Rzeszewski, M., Chagué-Goff, C., Cachão, M., Goto, K., Sugawara, D., 2012. Sediment sources and sedimentation processes of 2011 Tohoku-oki tsunami deposits on the Sendai Plain, Japan — insights from diatoms, nannoliths and grain size distribution. Sediment. Geol. 282, 40–56. https://doi.org/10.1016/j.sedgeo.2012.07.019.

Tashiro, A., Kogure, M., Nagata, S., Itabashi, F., Tsuchiya, N., Hozawa, A., Nakaya, T., 2021. Coastal exposure and residents' mental health in the affected areas by the 2011 Great East Japan Earthquake and Tsunami. Sci. Rep. 11, 16751 https://doi.org/10.1038/s41598-021-96168-z.

Timmons, E.A., Fisher, T.G., Hansen, E.C., Eisaman, E., Daly, T., Kashgarian, M., 2007. Elucidating aeolian dune history from lacustrine sand records in the Lake Michigan Coastal Zone, USA. Holocene 17, 789–801. https://doi.org/10.1177/0959683607080520.

Tuttle, M.P., Ruffman, A., Anderson, T., Jeter, H., 2004. Distinguishing tsunami from storm deposits in eastern North America: the 1929 Grand Banks tsunami versus the 1991 Halloween storm. Seismol Res. Lett. 75, 117–131. https://doi.org/10.1785/gssrl.75.1.117.

Urabe, J., Nakashizuka, T., 2016. Ecological Impacts of Tsunamis on Coastal Ecosystems. Lessons from the Great East Japan Earthquake. Springer.

Witkowski, A., Lange-Bertalot, H., Metzeltin, D., 2000. Diatom flora of marine coasts I. In: Lange-Bertalot, H. (Ed.), Iconographia Diatomologica, vol. 7. A.R.G Ganter Verlag K.G., Ruggell, p. 925.

Wood, S.N., 2017. Generalized Additive Models: an Introduction with R, second ed. Chapman and Hall/CRC.

Woszczyk, M., Tylmann, W., Jędrasik, J., Szarafin, T., Stach, A., Skrzypczak, J., Lutyńska, M., 2014. Recent sedimentation dynamics in a shallow coastal lake (Lake Sarbsko, northern Poland): driving factors, processes and effects. Mar. Freshw. Res. 65, 1102. https://doi.org/10.1071/MF13336.